Self-potential as a tool to assess groundwater flow in hydrothermal systems: A review

André Revil, A. Finizola, M. Gresse

Journal of Volcanology and Geothermal Research 437 (2023) 107788

Contents lists available at ScienceDirect

Journal of Volcanology and Geothermal Research

journal homepage: www.journals.elsevier.com/journal-of-volcanology-and-geothermal-research

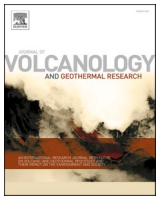

Self-potential as a tool to assess groundwater flow in hydrothermal systems: A review

A. Revil [a,*], A. Finizola [b,c], M. Gresse [d]

[a] Université Grenoble Alpes, Univ. Savoie Mont-Blanc, CNRS, UMR CNRS 5204, EDYTEM, 73370 Le Bourget du Lac, France
[b] Université de La Réunion, Laboratoire GéoSciences Réunion, F-97744 Saint Denis, France
[c] Université de Paris, Institut de Physique du Globe de Paris, CNRS, F-75005 Paris, France
[d] Research Institute of Earthquake and Volcano Geology, Geological Survey of Japan, AIST, Tsukuba, Japan

ARTICLE INFO

Keywords:
Self-potential
Groundwater flow
Hydrothermal systems
Streaming potential
Electrokinetic coupling

ABSTRACT

In hydrothermal systems associated with volcanic areas, the flow of groundwater generates an electrical current of electrokinetic nature, the so-called streaming current. This current is associated with the drag of the excess of charge located near the surface of the minerals, in the liquid pore water, in the so-called Gouy-Chapman diffuse layer. In turn, the streaming current generates an electrical field (the streaming potential) that can be remotely recorded at the ground surface of the Earth (or in wells) with a simple voltmeter and pairs of non-polarizing electrodes. A map of self-potential signals can be obtained at any scale using some specific procedures to correct for the drifting of the electrodes or error closures in the mapping of these signals at large scales (tens of kilometers). We first review the underlying physics of self-potential signals. Then we discuss forward and inverse modeling with specific examples pertaining to volcanic areas. Several case studies of large scale self-potential anomalies are discussed. We show how self-potential signals can be used to assess the pattern of groundwater flow in such hydrothermal systems. In addition, we discuss how transient hydro-mechanical disturbances can generate transient self-potential anomalies than can be, in turn, inverted to obtain information on the source of these signals including their localization and magnitude. The next grand challenge to monitor active volcanoes will be the combination of transient self-potential signals with time-lapse electrical conductivity and induced polarization tomography and hydromechanical simulation codes.

1. Introduction

Hydrothermal systems associated with volcanic areas are made up of *heat sources* and *sinks* and a heat exchanger between them. Heat source corresponds to magmatic chambers or a region of elevated heat flux for instance in areas of rifting. The heat sink is typically the atmosphere where the heat is exchanged through the ground surface. The heat exchanger itself corresponds to a compartmentalized geological system with clay caps (rich in smectite) acting as flow barriers and fluids that transfers their internal energy through a network of faults and open channels episodically reactivated through thermo-hydro-mechanical processes (e.g., Moore and Glaser, 2007; Reinsch et al., 2017; Lu, 2018; Kushnir and Loewer, 2020; Gascuel et al., 2020). In this paper, we are especially interested by high enthalpy hydrothermal systems (above 150–225 °C) associated with volcanism.

In the context of the exploration of such hydrothermal reservoirs, geophysical methods play a critical role. The self-potential method is a simple non-intrusive and passive geophysical method that is considered to be one of the oldest methods in geophysics (see Fox, 1830; Ahmad, 1969; Bogoslovsky and Ogilvy, 1973; Sill, 1983). One specific advantage of the self-potential method is that it can be used to assess non-intrusively the flow of the groundwater (Keller, 1981; Spies and Frischknecht, 1992; Vozoff, 1992; Huenges, 2010; Jolie et al., 2021). It has also a long history in the study of hydrothermal systems (e.g., Poldini, 1938, 1939; Zohdy et al., 1973; Anderson and Johnson, 1976). There are no other geophysical methods that can be used as such a non-intrusive groundwater flow sensor.

In self-potential, the earth electrical field is passively measured at the ground surface and a profile or a map of the electrical potential distribution (expressed usually in millivolts, mV) is obtained. Such measurement can be done with a high-input impedance voltmeter (typically $\geq$100 MΩ) and a pair of non-polarizing electrodes (such as $Cu/CuSO_4$,

* Corresponding author.
E-mail address: andre.revil@univ-smb.fr (A. Revil).

https://doi.org/10.1016/j.jvolgeores.2023.107788
Received 12 March 2022; Received in revised form 4 March 2023; Accepted 11 March 2023
Available online 18 March 2023

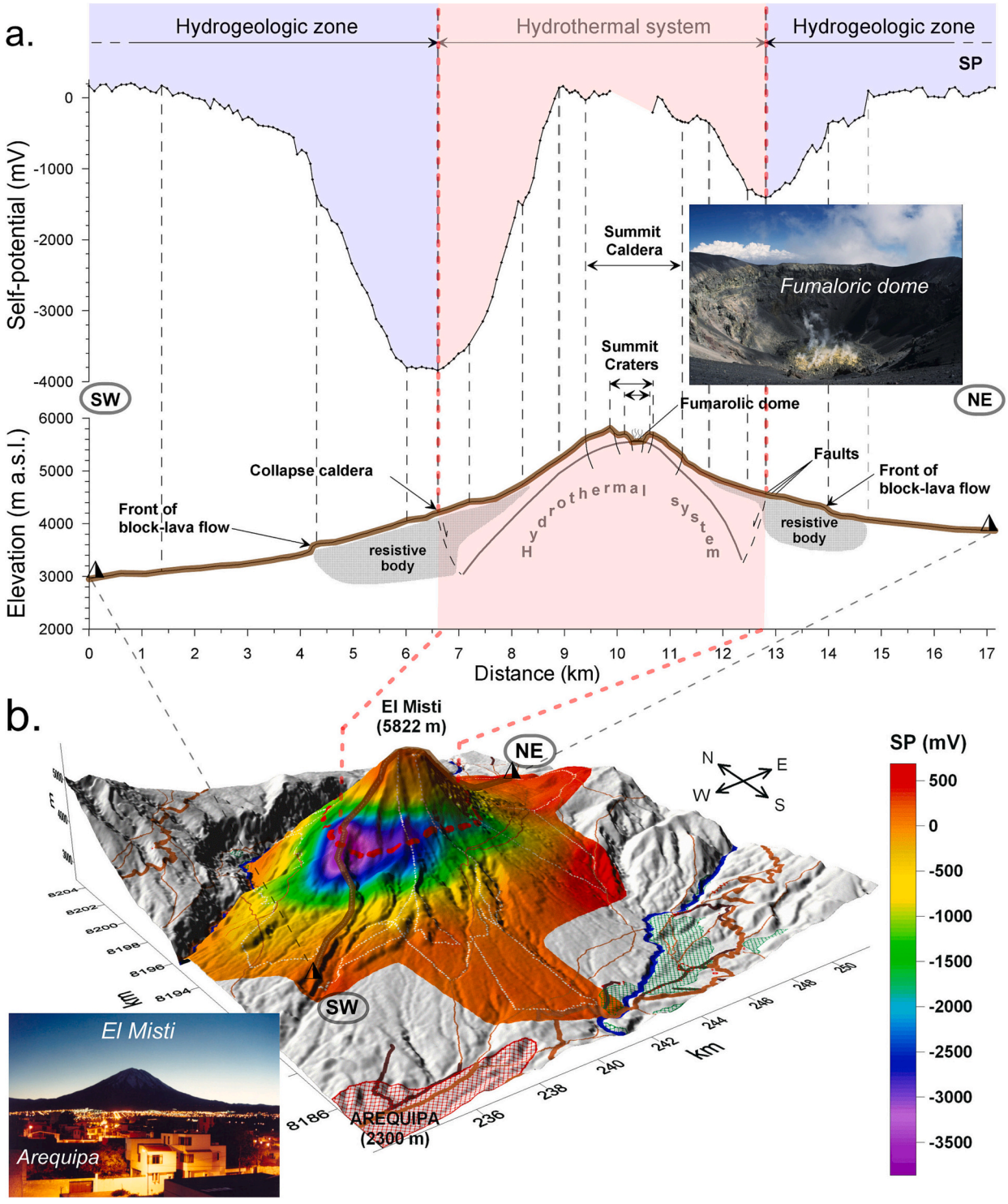

Fig. 1. Self-potential anomaly over El Misti volcano in Peru. a. Self-potential profile with respect to the structure of the volcano. The hydrothermal system is associated with a positive self-potential /elevation gradient,. The classical self-potential "W" shape displays a hydrothermal system of 6 km in diameter. b. Self-potential map in 3D view of El Misti volcano. SP stands for self-potential (modified from Finizola et al., 2004).

Ag/AgCl or Pb/$PbCl_2$ electrodes, e.g., Petiau and Dupis, 1980; Petiau, 2000). The equipment is therefore relatively inexpensive and simple. Some review of the self-potential methods can be found in Jouniaux et al. (2009) and Revil (2010).

It is known since the 19th century that the flow of water through a porous material or a capillary generates an electrical current of electro-kinetic nature, i.e., related to the relative displacement between the charged mineral surface and the electrical diffuse layer coating this surface (e.g., Quincke, 1859). The resulting electrical field is called the streaming potential (Bull and Gortner, 1932; Wurmstich and Morgan, 1994). In the realm of hydrogeophysics, the self-potential method can be used to detect groundwater flow (e.g., Poldini, 1938; Poldini, 1939; Revil et al., 2005a, 2005b; Suski et al., 2006) with applications to dams and embankments (e.g., Bogoslovsky and Ogilvy, 1973; Gex, 1980; Bolève et al., 2011) and pumping tests in wells (e.g., Semenov, 1980; Malama et al., 2009a, 2009b; Soueid et al., 2016; Soueid Ahmed et al., 2016).

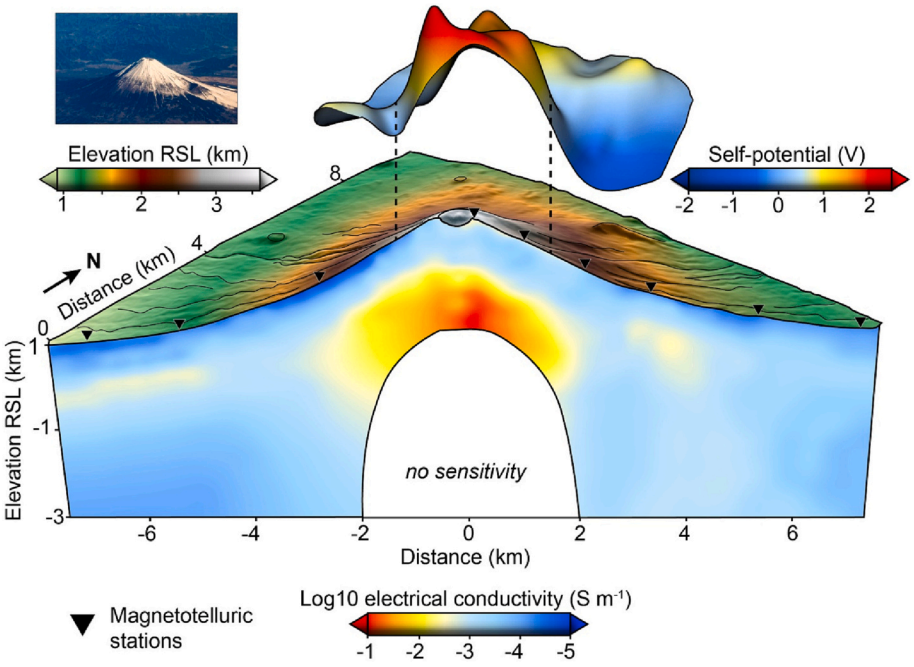

Fig. 2. 3-D self-potential anomaly of Mt. Fuji volcano (Japan) and its associated 2-D conductive structure (modified from Aizawa, 2004, and Aizawa et al., 2005). The magnetotelluric stations used to obtain the conductivity structure of the volcano are reported with black triangles. The topography of the volcano overlain is given with Respect to the Sea Floor (RSL). The positive anomaly (+2 V) is induced by the upflow of the hydrothermal fluids associated with the hydrothermal system, and the presence of a conductive zone (10^{-1}–10^{-2} S·m^{-1}) beneath the edifice.

For volcanoes, examples of the self-potential profiles and maps are presented in Figs. 1 to 3 for Misti volcano in Peru, and Mt. Fuji and Miyakejima volcanoes in Japan. For these volcanoes and others, large-scale anomalies of hundreds of millivolts can be observed over several kilometers (Ishido et al., 1997, Aubert et al., 1990; Aizawa, 2000; Zlotnicki and Nishida, 2003; Finizola et al., 2004; Barde-Cabusson et al., 2009b; Barde-Cabusson et al., 2012; Villasante-Marcos et al., 2014; Gonzales et al., 2014; Gresse et al., 2021). Self-potential anomalies can be related to the flow of the groundwater in shallow unconfined aquifers (Bogoslovsky and Ogilvy, 1973; Fournier, 1989; Suski et al., 2004, 2006), in the vadose zone (Aubert and Dana, 1994), along permeable paths in faults (Aubert and Dana, 1994; Revil and Pezard, 1998a, 1998b; Finizola et al., 2002, 2003; Hase et al., 2005; Bennati et al., 2011) or through free convection in high permeability reservoirs (Revil et al., 1999a, 1999b).

Transient self-potential signals can also be recorded with a network of non-polarizing electrodes in the form of time-change of the electrical field (e.g., Moore and Glaser, 2007; Barde-Cabusson et al., 2009a; Zlotnicki and Nishida, 2003; Matsushima et al., 2017). These fluctuations can be related to change in groundwater flow associated with the thermal or thermo-hydro-mechanical disturbances e.g., through thermal pressurization (Haas et al., 2013; Kuwano et al., 2015; Chaput et al., 2019). The self-potential method can therefore complement seismological data to decipher and monitor the plumbing system of hydrothermal fields (Mahardika et al., 2012).

In this paper, we review the use of the self-potential method in the context of hydrothermal reservoirs associated with volcanoes. We first discuss the underlying physics of the self-potential signals. Then we discuss the methodology that can be used to map these signals in the field. We present the two main types of self-potential signals associated with (i) groundwater flow (streaming potential, Quincke, 1859) and (ii) the self-potential contribution associated with ore bodies (electro-redox contribution, e.g., Stoll et al., 1995). Forward numerical modeling of the self-potential signals can be done in concert with groundwater flow modeling (e.g., Wilt and Corwin, 1989; Sheffer and Howie, 2003). Since the underlying physics is known and validated, inverse modeling of the self-potential signals can be done in the realm of potential field techniques or coupled flow approaches either with stochastic or deterministic methods. Finally, we discuss case studies with the goal of showing pertinent self-potential surveys at various scales and their interpretation.

2. Underlying physics

Figs. 1 to 3 show that large-scale self-potential anomalies (up to several volts) are associated with the hydrothermal systems of volcanoes. In order to understand these signals recorded at the meso-scale, we need first to explore their underlying physics at the microscale. In this section, we describe the two main contributions of the self-potential signals in hydrothermal systems: (i) the contribution associated with groundwater flow, the so-called streaming potential contribution, and (ii) the contribution associated with the presence of ore bodies (the so-called geo-battery or electro-redox mechanism). Two other contributions exist. The first is related to a gradient in temperature (the so-called thermoelectric effect, see Leinov et al., 2010; Revil et al., 2013a, 2016; typically characterized by a thermoelectric coupling coefficient in the range from −0.25 to 1.5 mV/°C, with a mean value of 0.2 mV/°C, see Zlotnicki and Nishida, 2003, from the studies of Yamashita, 1961; Nourbehecht, 1963; Dorfman et al., 1977). The second contribution is associated with the gradient in the chemical potential of the charge carriers in isothermal conditions (the so-called membrane polarization effect, see Revil, 1999; Maineult et al., 2005, 2006 and references therein). This second contribution is also rather modest (usually few tens of millivolts at most). These two additional contributions can be safely neglected for the applications discussed in the present paper and therefore will not be further reviewed below.

2.1. Groundwater flow contribution

The surface of all minerals in contact with water is reactive and becomes electrically charged in contact with an aqueous solution (e.g., Avena and De Pauli, 1998; Pokrovsky et al., 1999). Typical reactive surface sites are for instance associated with hydroxyl groups >OH (> refers to the crystalline framework, O oxygen and H hydrogen). These groups behave as acid/base species. It generally results in a net negative charge density located on the mineral surface (especially for silicates and alumino-silicates) under classical pH conditions (weakly acidic to near neutral, typically in the pH range 4–8, see Fig. 4). Some ions from

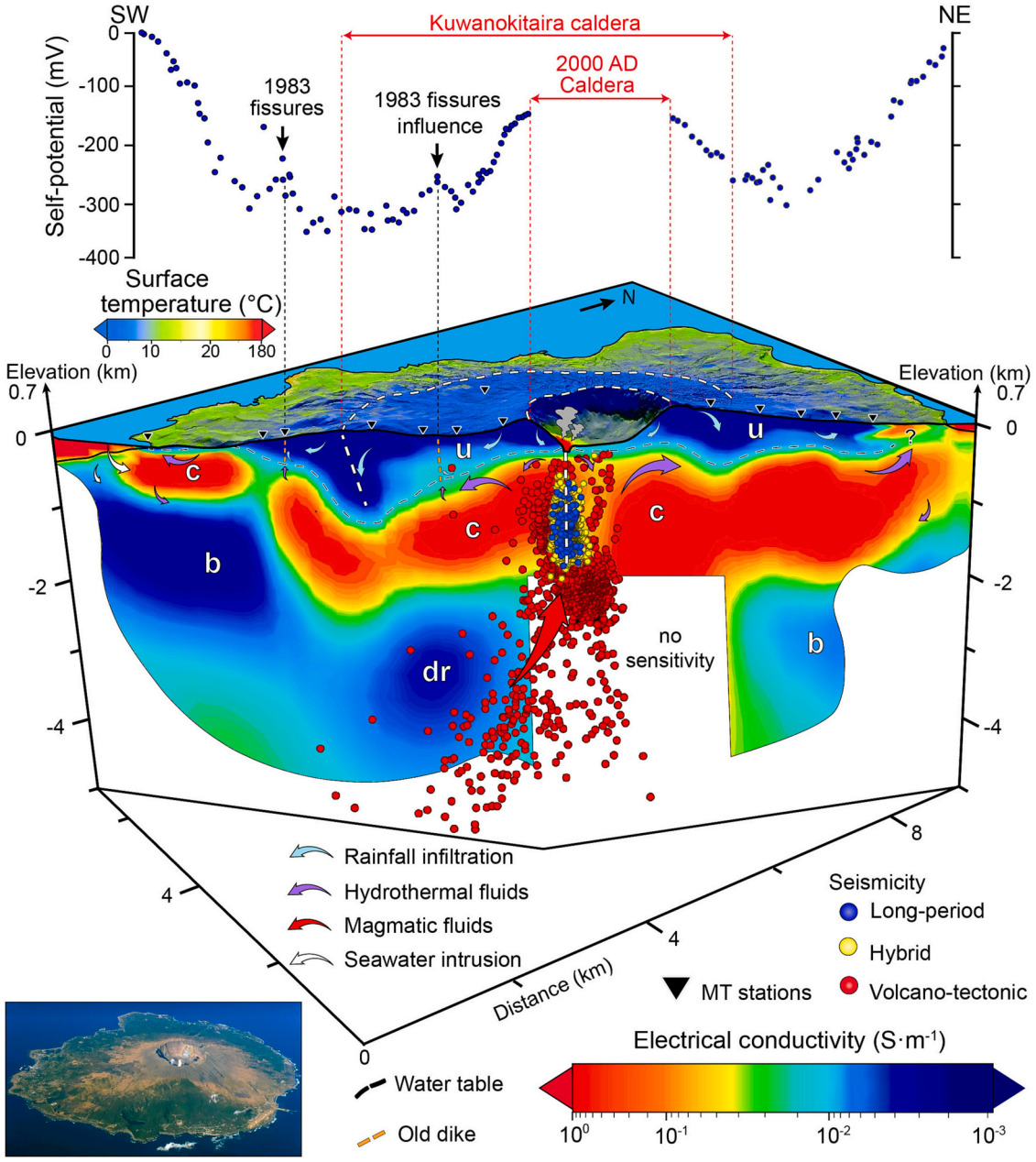

Fig. 3. Cross-section of the electrical conductivity model of Miyakejima volcano (SW–NE) with hypocenters, overlain with surface temperature map (in °C) and self-potential (in mV). Units are 'u' = unsaturated deposits (4.5×10^{-4}–7.7×10^{-3} S·m^{-1}), 'c' = clay (smectite-rich) cap (3.3×10^{-2}–0.4 S·m^{-1}), 'b' = basement rocks (1×10^{-3}–1.4×10^{-2} S·m^{-1}), and 'dr' stands for deep resistor' (2×10^{-3}–5.10^{-3} S·m^{-1}). The shallow seismicity reveals the volcano conduit. Deep seismicity mostly consists of volcano-tectonic events (red dots) that can be connected to the upwelling of hot water in a network of cracks. This upwelling is associated with a positive self-potential anomaly. Modified from Gresse et al. (2021). (For interpretation of the references to colour in this figure legend, the reader is referred to the web version of this article.)

the liquid pore water are weakly or strongly sorbed (without the formation of covalent bounds) on the surface of the minerals forming the so-called Stern layer. In addition to this Stern layer, there is a second layer called the Gouy-Chapman (diffuse) layer in which the ions obey Poisson-Boltzmann distributions associated with the Coulombic interactions with the charge located on the mineral surface (Fig. 4). The Stern layer and the Gouy-Chapman layer formed the so-called electrical double layer coating the surface of the minerals. The sum of the charge densities of the mineral surface, the Stern layer and the diffuse layer is equal to zero (global electroneutrality condition). This implies however that there is excess of electrical charge in the liquid pore water, which is therefore not electroneutral. The volumetric charge density of the diffuse layer is mobile.

The drag of the (mobile) excess of charge in the liquid pore water by the flow of the pore water generates, by definition, a (source) current density of advective nature called the streaming current density $\mathbf{j}_S$ (in A m^{-2}, Helmholz, 1879, see Fig. 4). This current acts as a source of electromagnetic disturbances in the Maxwell equations. The resulting electrical field component is called the streaming potential (Revil et al., 2003).

2.2. Ore body contribution

In addition to the streaming current, another strong contribution exists when a metallic body crosses an area characterized by a gradient in the redox potential (Sato and Mooney, 1960; Furness, 1994; Stoll

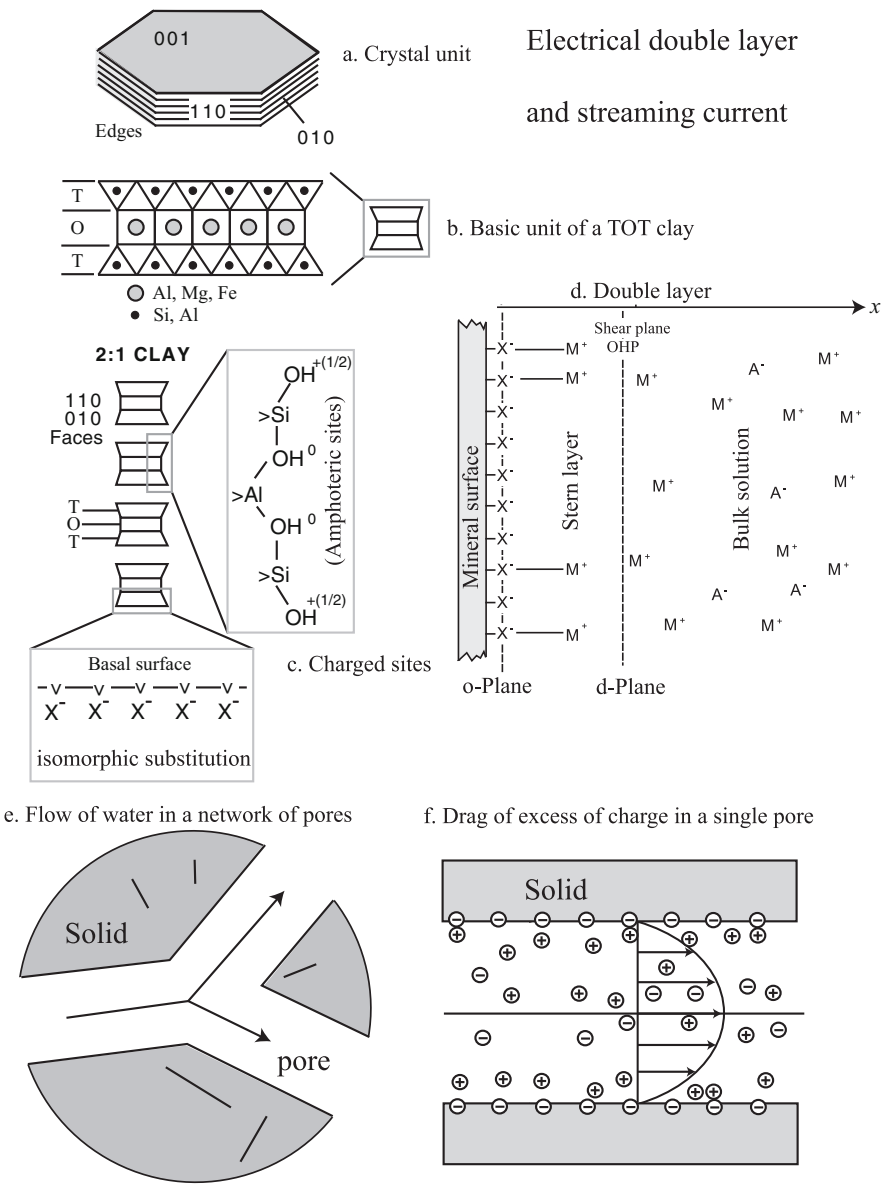

Fig. 4. Electrical double layer on the surface of clay minerals. a. A clay crystal is characterized by different crystalline planes characterized by their electrical charge. b. In this sketch, the clay is based on a TOT structure with T the tetrahedral layer based on the chemistry of silicium Si (with possible isomorphic substitution with aluminium Al) and O the octahedral layer based on the chemistry of aluminium (with possible isomorphic substitution with magnesium Mg and iron Fe). c. The sites are usually amphoteric sites on the crystal edges (i.e., the charge is pH-dependent) and charges associated with isomorphic substitutions on the basal planes (which are pH-independent). d. the electrical double layer is formed by the Stern layer of sorbed counterions and the diffuse layer. e. Flow of water in the pore space. f. Streaming current density j_S produced by the drag of the mobile excess of charge located in the pore space by the flow of the pore water.

et al., 1995; Rittgers et al., 2013 and references therein). The redox potential characterizes the ability of half-redox reactions to provide or accept electrons in the pore water keeping in mind that electrons do not exist as such in the liquid pore water (at the opposite of protons). This geobattery component is therefore equivalent to a natural battery that would discharge current in the conductive Earth (Mendonça, 2008). It follows that any ore body is responsible for a static self-potential anomaly at the ground surface, generally negative, and typically amounting few hundred of millivolts. In the present paper, we are not interested by this contribution, but we should be aware that it exists. Indeed since the self-potential method is passive, all the existing contributions are recorded together including this geo-battery effect and superposition principle applies. In addition ore mineralization is ubiquitous in hydrothermal fields (Goodfellow, 2007). That said, disseminated pyrite or magnetite mineralization, both common hydrothermal alteration products, would have no strong impact on self-potential signals. Massive sulfide deposits are usually characterized by negative self-potential anomalies (e.g., Su et al., 2022). The induced polarization method can be used to localize ore bodies and predict their self-potential anomalies. Combining induced polarization with self-potential is an area of active research.

3. From laboratory to field scales

In this section, we review the metrology used to describe the streaming current and streaming potential first in the laboratory and then in the field. At the laboratory scale, we describe a typical streaming potential experiment performed on a core sample, which has first to be characterized in terms of porosity, cation exchange capacity (CEC), permeability, and electrical conductivity. Then we discuss the approach used to get accurate field data at the scale of several kilometers.

3.1. Laboratory scale

Classical streaming potential laboratory measurements are performed on rock samples (possibly unconsolidated) in order to characterize their so-called streaming potential coupling coefficient *C*. The experiments can be done at different temperatures, salinities, pore water composition and pH (Ishido and Mizutani, 1981; Revil et al., 1999a, 1999b) and saturation (Revil et al., 2007; Jackson, 2008, 2010). A core sample is placed between two reservoirs at two different fluid pressures. The simplest experiment is to impose different hydraulic heads in one reservoir and to keep the second reservoir a fixed lower hydraulic head

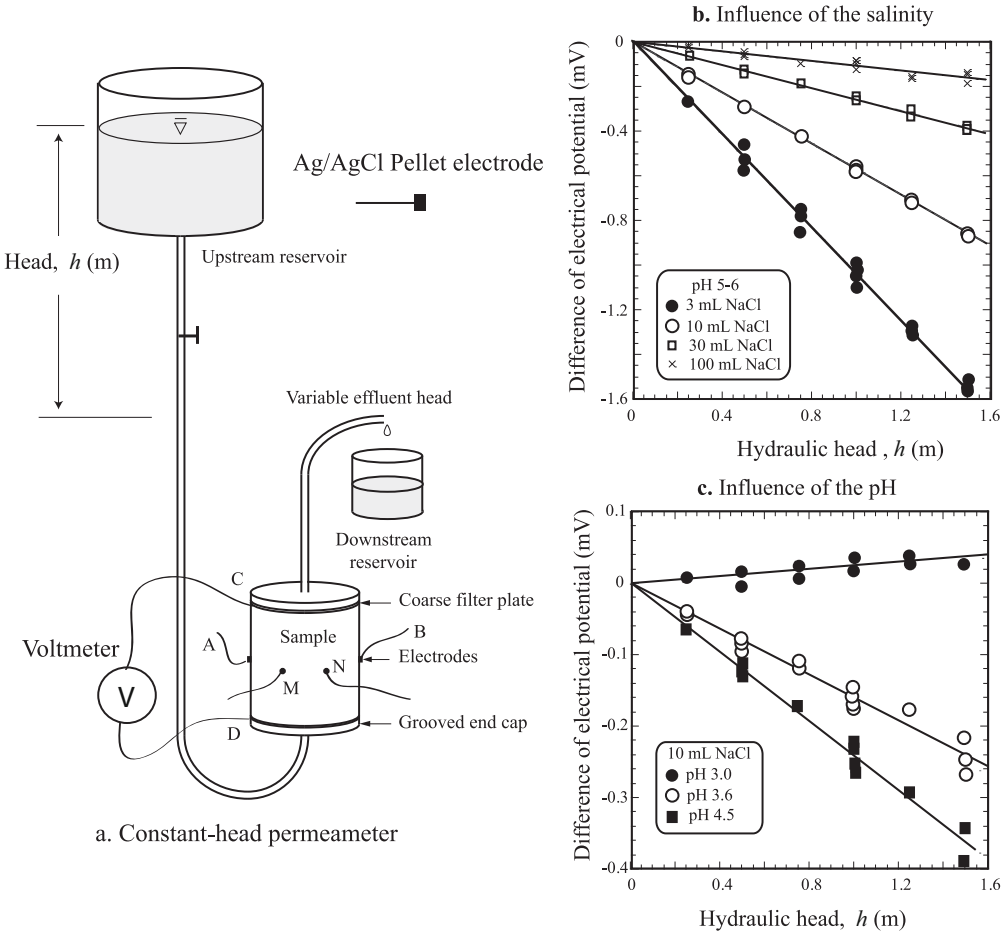

Fig. 5. Experimental setup to measure simultaneously the streaming potential coupling coefficient, the electrical conductivity and the permeability of a core sample. a. Constant head permeameter. Electrodes C and D are non-polarizable electrodes (e.g., Pellet-type Ag/AgCl electrodes) used to measure the streaming potential at the end-faces of the core sample. The electrodes A, B, M, N are the four electrodes used to measure the electrical conductivity (with induced polarization effect) on the side of the code sample. The flow of water through the core sample is used to determine the permeability. b. Influence of the pore water conductivity on the difference of electrical potential measured over the electrodes C and D. The coupling coefficient corresponds to the slope of these trends. c. Influence of the pore water pH on the difference of electrical potential measured over the electrodes C and D. The coupling coefficient corresponds to the slope of these trends. Modified from Revil et al. (2013b).

close to the atmospheric pressure (Fig. 5). The difference of electrical potentials at the two end-faces of the core samples is recorded as a function of the difference of (hydraulic) heads imposed over the core sample, and responsible for the flow of the pore water through the core sample. In turn, the flow of the pore water drags the excess of charge located in the liquid phase generating the streaming current described in Section 2.1 above. In such experiment, the total current density $\mathbf{j}$ is zero and the conduction current density $\sigma\,\mathbf{E}$ (σ is the electrical conductivity and $\mathbf{E}$ the electrical field) exactly balances the streaming current density $\mathbf{j}_S$.

The streaming potential coupling coefficient C (expressed in V m^{-1}) is simply defined as (see Fig. 5, see Pengra et al., 1999),

$$C = \left(\frac{\partial \varphi}{\partial h}\right)_{\mathbf{j}=0}. \tag{1}$$

where φ denotes the electrical potential (in Volt, $\mathbf{E} = -\nabla\varphi$ the electrical field in absence of induction in V m^{-1}) and h is the hydraulic head (in m). The streaming potential coupling coefficient can be also expressed in Volt per Pa (or MPa), i.e., with respect to the fluid pressure $p = \rho_w g h + \delta p$ where ρ_w denotes the mass density of water (kg m^{-3}), g is the acceleration of gravity (m s^{-2}), and δp the excess pressure (Pa) above or below the hydrostatic pressure. Rather than measuring the streaming potential coupling coefficient C, we can also directly measure the streaming current density $\mathbf{j}_S$ by short-circuiting the two end-faces of the core sample with platinum grids and using an Ampere meter (e.g., see for instance Fig. 1 in Erickson and Li, 2001).

There is a substantial amount of works dedicated to the upscaling of the local equations to obtain the macroscopic constitutive equations valid at a representative scale of the porous material (e.g., Pride, 1994, Revil and Linde, 2006). Recent pore scale models have analyzed the problem in terms of pore size distribution and the effect of the fractal dimension characterizing the self-affine (multi-scale) character of the texture of natural porous rocks (e.g., Jougnot et al., 2021). The streaming potential coefficient is also partly controlled by the chemistry of the pore water as underlined very early by the work of Ishido and Mizutani (1981). At normal pH conditions (in the range 4–8), the effective excess of charge in the pore water is positive (i.e., the electrical potential more is positive in the direction of the groundwater flow) and strongly controlled by the permeability of the porous material (Fig. 6). That said, at low pH values (below 4), the charge in the pore water can be null at a condition called the zero point of charge of the mineral surface. The excess of charge of the pore water can even be negative at very low pH values (see Ishido and Mizutani, 1981), typically under extremely acidic environment (<2, Ishido and Mizutani, 1981) or possibly at very elevated ionic strengths of the pore water (Alarouj et al., 2021a, 2021b).

3.2. *Mapping the self-potential field*

We discuss now a strategy to establish a map of the distribution of the electrical (self-) potential at the ground surface of the Earth. Reliable electrodes such as Petiau (Pb/$PbCl_2$) (Petiau and Dupis, 1980; Petiau, 2000), or Cu/$CuSO_4$ electrodes can be used to perform a self-potential survey on land (Fig. 7). The Petiau electrodes have the advantage to be considerably less sensitive to temperature fluctuations than Cu/$CuSO_4$ electrodes. In addition these electrodes are more suitable for continuous monitoring due to their lower drift characteristics. However, most existing models of Petiau electrodes cannot be opened and are more challenging to use for mapping by comparison with Cu/$CuSO_4$

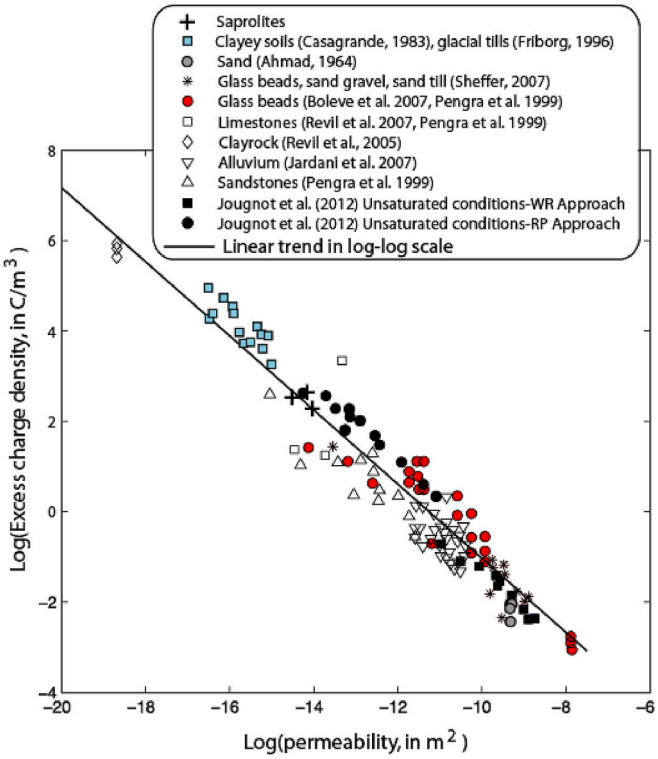

Fig. 6. Plot of the effective charge density versus permeability. The trend is obtained using a broad collection of cores displaying various lithologies. This indicates the universal character of the trend. The pore water are characterized by near neutral pH conditions (pH comprised between 5 and 8). The effective charge densities are obtained from the measurements of the streaming potential coupling coefficients. The experimental data are from Ahmad (1964), Casagrande (1983), Friborg (1996), Pendra et al. (1999), Revil et al. (2005, 2007), Bolève et al. (2007b), Jardani et al. (2007), Sheffer (2007), and Jougnot et al. (2012).

electrodes.

One of the two non-polarizing electrodes is used as a reference. This electrode is buried at a fixed location called the reference station. This reference electrode is kept in a small hole filled or not with bentonite mud (Fig. 7). If bentonite is required to improve the contact between the reference electrode and the ground, the presence of the bentonite mud modifies the electric potential at the contact between the electrode and the ground. Therefore the potential of this station is arbitrary, and should not be used as a point (e.g., with zero potential) in performing the self-potential map. The second non-polarizing electrode is used to sample the electric potential at the ground surface of the Earth. Adding salty water in order to improve the coupling between the scanning (roving) electrode and the ground should also be avoided because its evaporation may generate spurious potential changes over time. If possible, self-potential measurements should be performed during seasons or periods of wet soil conditions and the contact resistance between the roving electrode and the ground should be always smaller by a factor of at least 100 with respect to the internal resistance of the voltmeter. The roving electrode is used to measure the electric potential at a set of stations, referenced in space with a GPS (Global Positioning System). Both prior to and after the survey, the difference of electrical potential between the reference electrode and the roving electrode is measured by putting the electrodes in contact one against the other. A drift of 2 mV/day is generally considered acceptable for a self-potential survey. The potential map retrieved is, therefore, a map relative to the (unknown) potential at the base station if bentonite mud is used for this station. Only the electric field, i.e., the gradient of the electric potential, is well-defined outside the reference electrode.

An insulated (copper) cable is used for large-scale self-potential surveys (Fig. 7). The gauge of the cable does not matter. Its length is typically in the range 200 to 700 m for logistical reasons but also because the cable is not shielded. Self-potential profiles consist of one base station chosen as the reference and measurements are performed with a roving electrode at different secondary stations (for instance every 5, 10, or 20 m along the curvilinear ground surface). To extend the measurements at the end the cable, the last roving electrode became the new base station (see details of the procedure in Barde et al., 2021). At the end of each acquisition, the self-potential values are summed from reference to reference, to insure the continuity of the signal along the profile. Fig. 8 presents a 6-km-profile built using this principle.

In order to build a large scale self-potential map, a methodology is presented in Fig. 9. We perform imbricated self-potential loops. For each loop, we proceed like for a profile except that the profile is closed on itself. Therefore we can check at the end the existence of a closure error. The circulation of the electrical field should be zero along a closed loop performed at the ground surface; in other words, the sum of the drop potentials along a closed loop is zero. This strategy is described in Fig. 9. Closing each loop and correcting for their potential closure errors is an important step to avoid accumulating errors toward the end of the profiles (closure errors can reach hundreds of millivolts). Not closing the loops produces wrong self-potential maps with anomalies located at the end of the lines (a striking example is shown in Figs. 1 and 3 in Di Maio et al., 1998).

The correction procedure along a closed loop including several self-potential base stations is explained in Fig. 10. The self-potential measurements are by nature discontinuous each time a base station is used (the potential at the first station of the survey is set to zero). The first correction has to be used to insure the continuity of the electrical potential using the first base station of the profile as a global base station for the entire loop. The second correction corrects for the closure error along the loop as mentioned above.

A third strategy used in the marine environment or in lakes, is to directly measure the electrical field (not the electrical potential) by continuously recording the difference of potential in different directions (e.g., see Zhu et al., 2020, for self-potential measurements at the sea floor for an application to ore deposits). Note that around a volcano, lakes and rivers do not constitute equipotentials because their conductivity is not high enough to short-circuit the electrical potential response.

Finally for long profiles with no closure, such as shown in the present paper, great care should be taken in the way the change of base station is done. At each change in the base station, it is a good practice to survey the last 5 self-potential stations done prior the change to be sure about the drop of potential that should be applied to the new base station is correct. The new base station is also setup on the side of the profile itself and its electrical potential not use in the self-potential profile itself.

4. Forward and inverse modeling

Now that we have quickly reviewed the basic principles pertaining to the underlying physics of the streaming potential, we can review how this physics can be implemented to forward model the self-potential signals associated with groundwater flow using the approach first developed by Sill (1983). Then, we will discuss how the inverse modeling can be done in a very simple way to determine the pattern of groundwater flow following the approach developed by Jardani et al. (2007, 2008) and Revil and Jardani (2013).

Fig. 11 shows typical self-potential anomalies associated with groundwater flow scenarii. This includes the upward (Type I) or downward (Type II) of groundwater or the flow of water along a shallow aquifer (Type III). Type III is often called the “topographic effect” on volcanoes with strong topographies. Two other types of groundwater flow (Types V and VI in Fig. 11) show that different ground water flow patterns can yield the same self-potential distribution. Therefore

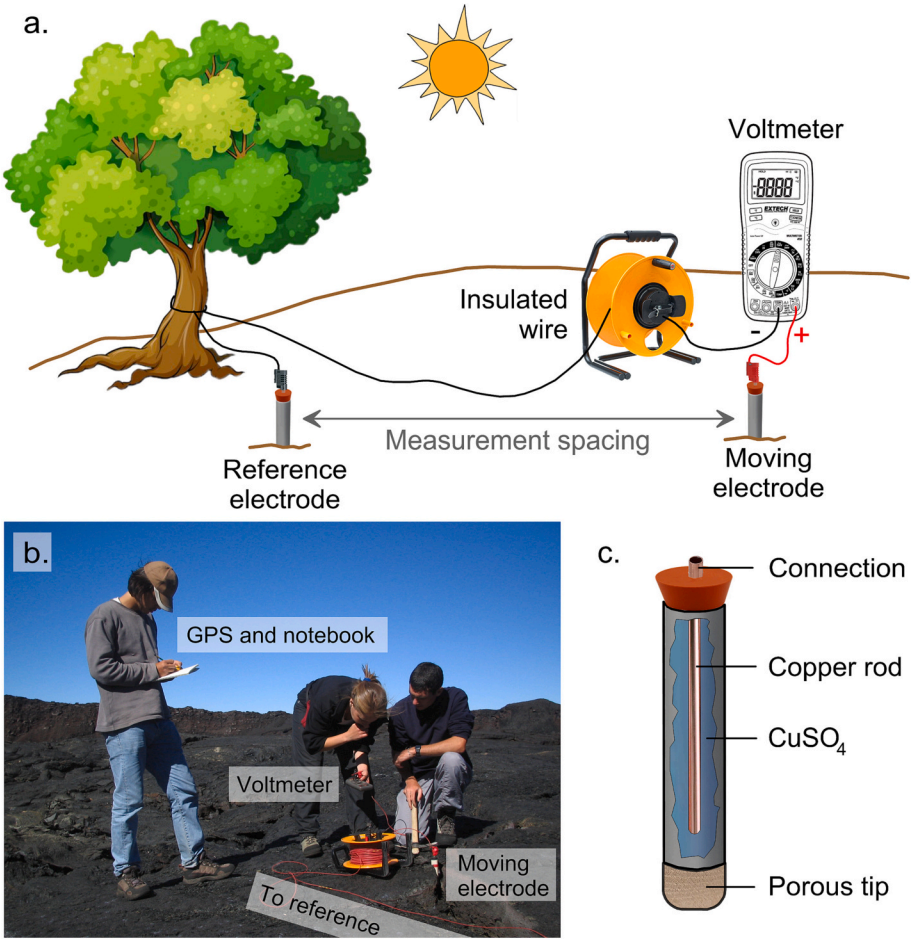

Fig. 7. Typical configuration for a self-potential survey with a base electrode used as the reference and a roving electrode for the field measurements (modified from Barde-Cabusson et al., 2021). The cable can be 500 m-long. A GPS (Global Positioning System) is used to measure the position of the stations where the self-potential is measured.

inverting the self-potential data to retrieve the groundwater flow is a challenging task since different patterns of ground water flow can produce the same self-potential anomalies at the ground surface.

4.1. Forward modeling: static groundwater flow problems

In porous media, the total current density $\mathbf{j}$ ($A{\cdot}m^{-2}$) is the sum of two contributions (Sill, 1983):

$$\mathbf{j} = \sigma\,\mathbf{E} + \mathbf{j}_s, \tag{2}$$

where σ ($S{\cdot}m^{-1}$) denotes the electrical conductivity of the porous material (see Waxman and Smits, 1968; Revil and Florsch, 2010). It is related to the conductivity of the pore water (see Sinmyo and Keppler, 2016; Guo and Keppler, 2019; Watanabe et al., 2021, for hydrothermal systems) and to the alteration though the cation exchange capacity of clays and zeolites (Waxman and Smits, 1968). The first term of equation (2) $\sigma\,\mathbf{E}$ represents the conductive current density originating from the electromigration of ions in the porous material, $\mathbf{E}$ denotes the electrical field, and $\mathbf{j}_s$ denotes the streaming current density (Fig. 4e and f). Regarding the physics pertaining to the description of the electrical conductivity in volcanic areas and hydrothermal systems, the readers are directed to the recent review by Revil and Gresse (2021).

In the quasi-static limit of the Maxwell equation, the electrical field is decoupled from the magnetic field and we have,

$$\nabla \times \mathbf{E} = 0 \Rightarrow \mathbf{E} = -\nabla\varphi \tag{3}$$

where φ denotes the electrical potential (in V). Bolève et al. (2007a) write the streaming (source) current density as the product of an effective excess of charge in the pore water (shown as a function of permeability in Fig. 6) and the Darcy velocity (e.g., Revil and Jardani, 2013):

$$\mathbf{j}_S = \widehat{Q}_V(s_w)\dot{\mathbf{w}} \tag{4}$$

where $\dot{\mathbf{w}}$, in unsaturated conditions, denotes the filtration velocity (Darcy velocity in $m\ s^{-1}$, i.e., the flux density of the pore water). The volume-averaged filtration displacement $\mathbf{w}$ is given by,

$$\mathbf{w} = s_w\phi(\mathbf{u}_w - \mathbf{u}) \tag{6}$$

where s_w denotes the water saturation ($s_w = 1$ at saturation), ϕ the connected porosity ($\theta = s_w\phi$ is the volumetric water content), and $\mathbf{u}_w$ and $\mathbf{u}$ the water phase and solid displacements, respectively. In the quasi-static limit of the Mawxell equations, the conservation equation for the total current density is given by,

$$\nabla{\cdot}\mathbf{j} = 0 \tag{5}$$

i.e., the current density is conservative. Combining Eqs. (2) to (5), the self-potential field φ is governed by a Poisson equation (Jardani and Revil, 2009a, 2009b; Revil and Jardani, 2013),

$$\nabla{\cdot}(\sigma\nabla\varphi) = \nabla{\cdot}(\widehat{Q}_V\dot{\mathbf{w}}) \tag{6}$$

$$\nabla^2\varphi = -\nabla ln\sigma{\cdot}\nabla\varphi + \frac{1}{\sigma}\nabla{\cdot}(\widehat{Q}_V\dot{\mathbf{w}}) \tag{7}$$

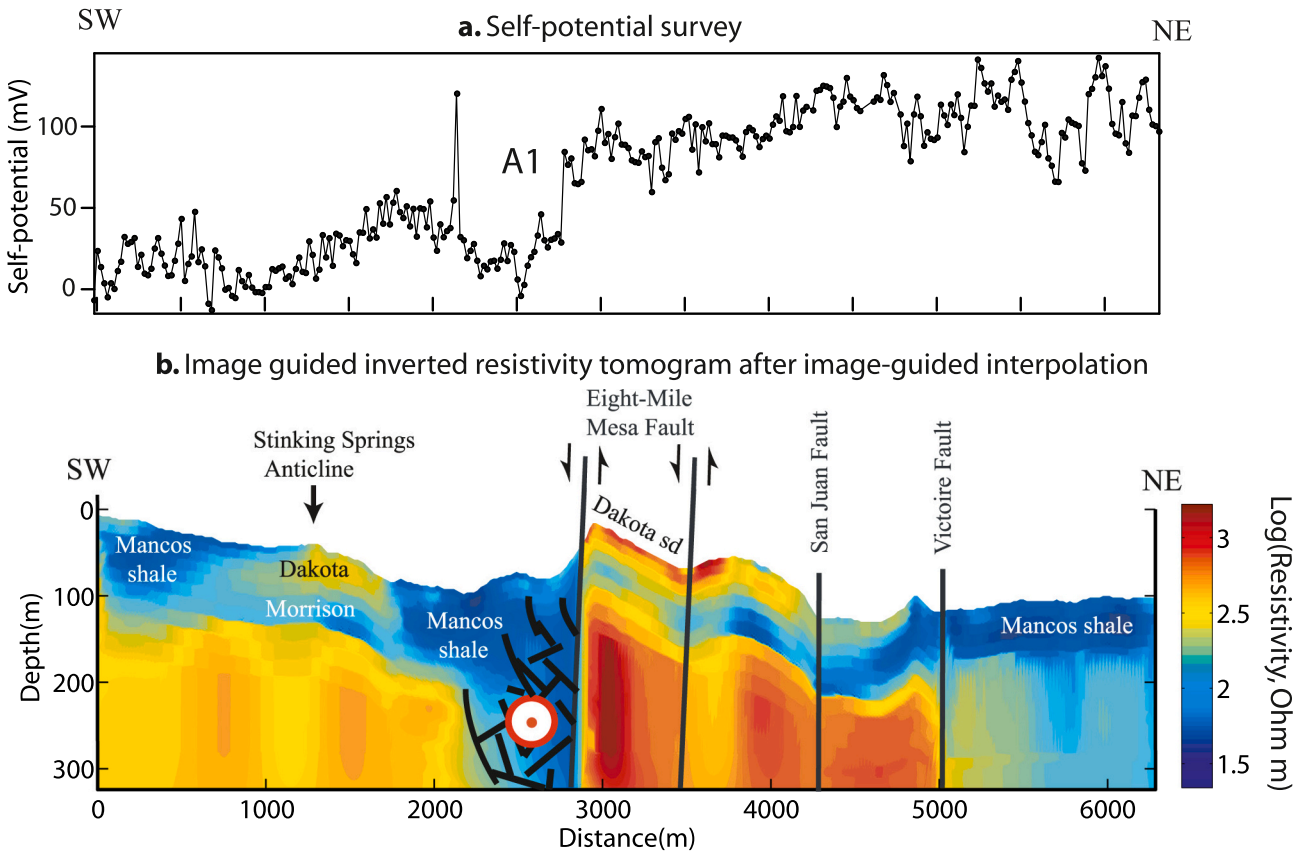

Fig. 8. The anomaly A1 (Type V) reflects the flow of hot water in the fractured hanging wall of the Eight-Mile Mesa fault (Colorado). a. Self-potential anomaly. b. Resistivity tomography (using an image-guided inversion) with the hydrogeological interpretation in terms of groundwater flow. The red arrow indicates flow normal to the plane of the section. (For interpretation of the references to colour in this figure legend, the reader is referred to the web version of this article.)

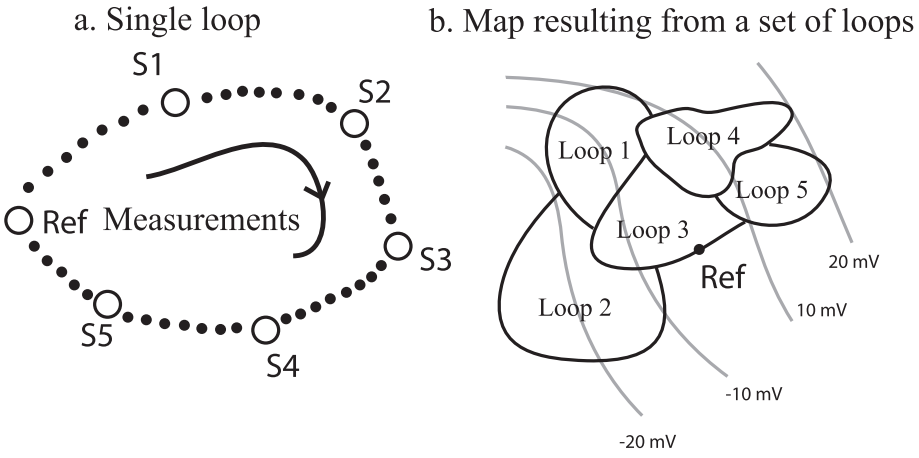

Fig. 9. Large scale self-potential mapping. Mapping over the ground surface using a closed loop approach combined with a leap-frog approach. a. Sketch shows a single loop. S0 denotes the first base station (which can be or not the reference station). Measurements are performed along the self-potential stations characterized by the small filled circles. At some point, a new base station is established S1 (which is not necessarily the new reference) and so on. The potential distribution can be reconstructed along the loop respecting the fact that the self-potential loop should be closed. A closure error correction should be applied to the data. b. Self-potential map built by combining the information on several imbricated loops and using one of the base stations as reference for the entire map. The black plain lines denote the self-potential loops while the grey lines denote the electrical equipotentials obtained for instance by kriging the self-potential data.

The right-hand side of Eq. (6) corresponds to the self-potential source term for the generation of electrical disturbances associated with the Darcy velocity distribution and the heterogeneity in the distribution of the charge density $\widehat{Q}_V$. Eq. (7), easily obtained from Eq. (6), shows that the self-potential anomalies are also modulated by the distribution of the electrical conductivity (secondary sources). This explains that the self-potential method can be used as a non-intrusive ground water flow sensor (Revil and Jardani, 2013, 2017). Therefore to invert self-potential signals, the electrical conductivity distribution needs to be known to distinguish primary (last term of Eq. (7)) to secondary sources associated with conductivity gradients (see Su et al., 2022 for a state-of-the art discussion on this point).

Obtaining the flow field $\dot{\mathbf{w}}$ implies to solve a groundwater flow problem in saturated or unsaturated conditions, in steady state or transient conditions, and using simplified or complex rheologies to model the deformation of the grain skeleton. Solving the groundwater flow problem (typically a non-linear diffusion equation) and the elliptic equation corresponding to Eq. (6) can be done with any type of numerical method. Usually, we use the finite element technique but this is a matter of task.

From Eqs. (2) and (4) and the definition of the streaming potential coupling coefficient, the relationship between this volumetric charge

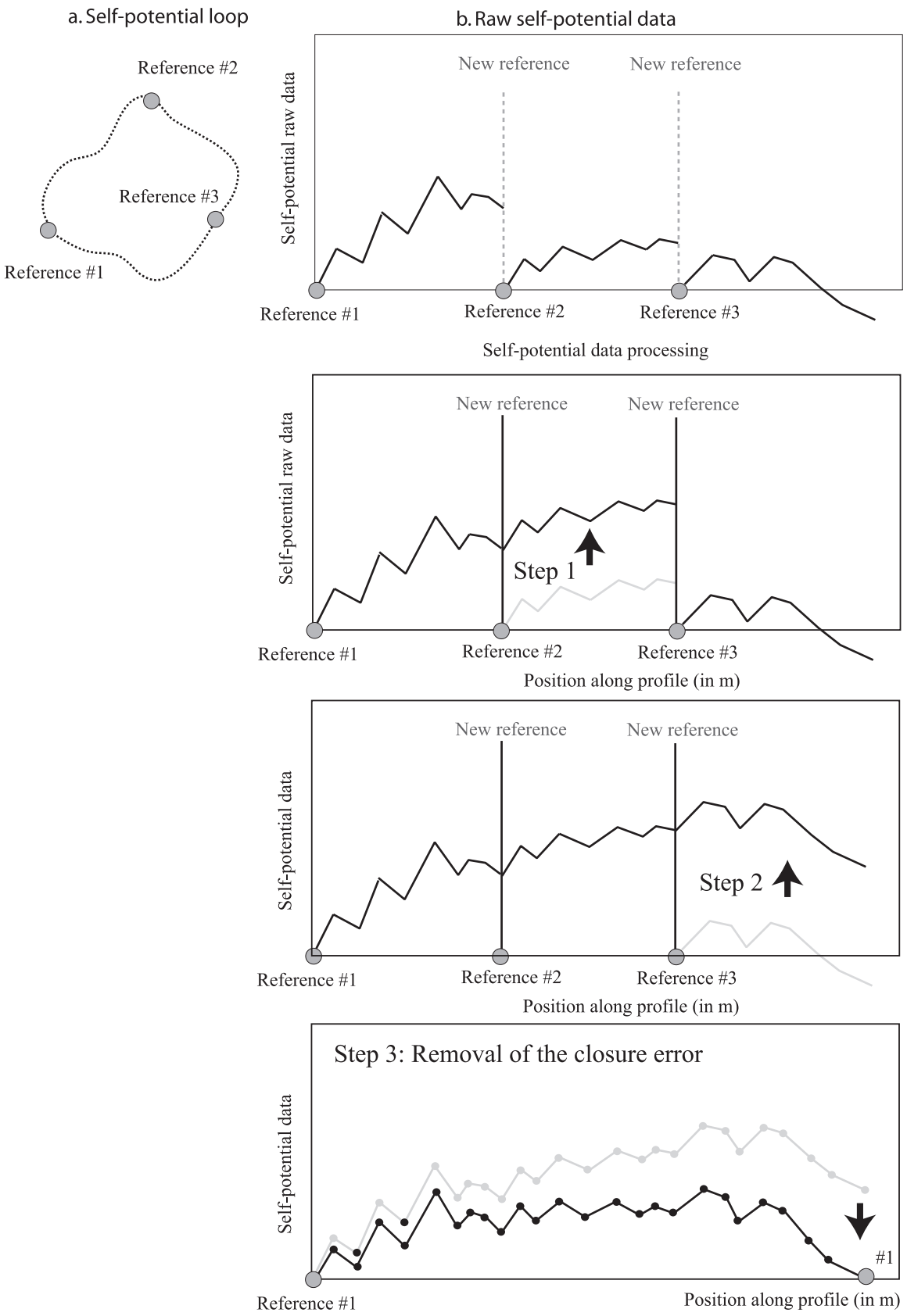

Fig. 10. Self-potential profile along a closed loop with a total of three base stations used as local references. a. Sketch showing the closed loop with the position of the references (base stations). b. Raw (acquired) self-potential profile. The corrections for the raw self-potential profile along a closed loop involve a series of steps. In the first set of step, the potential is set continuous at each change of base station. The closure error is removed at the last step in order to produce a consistent self-potential profile.

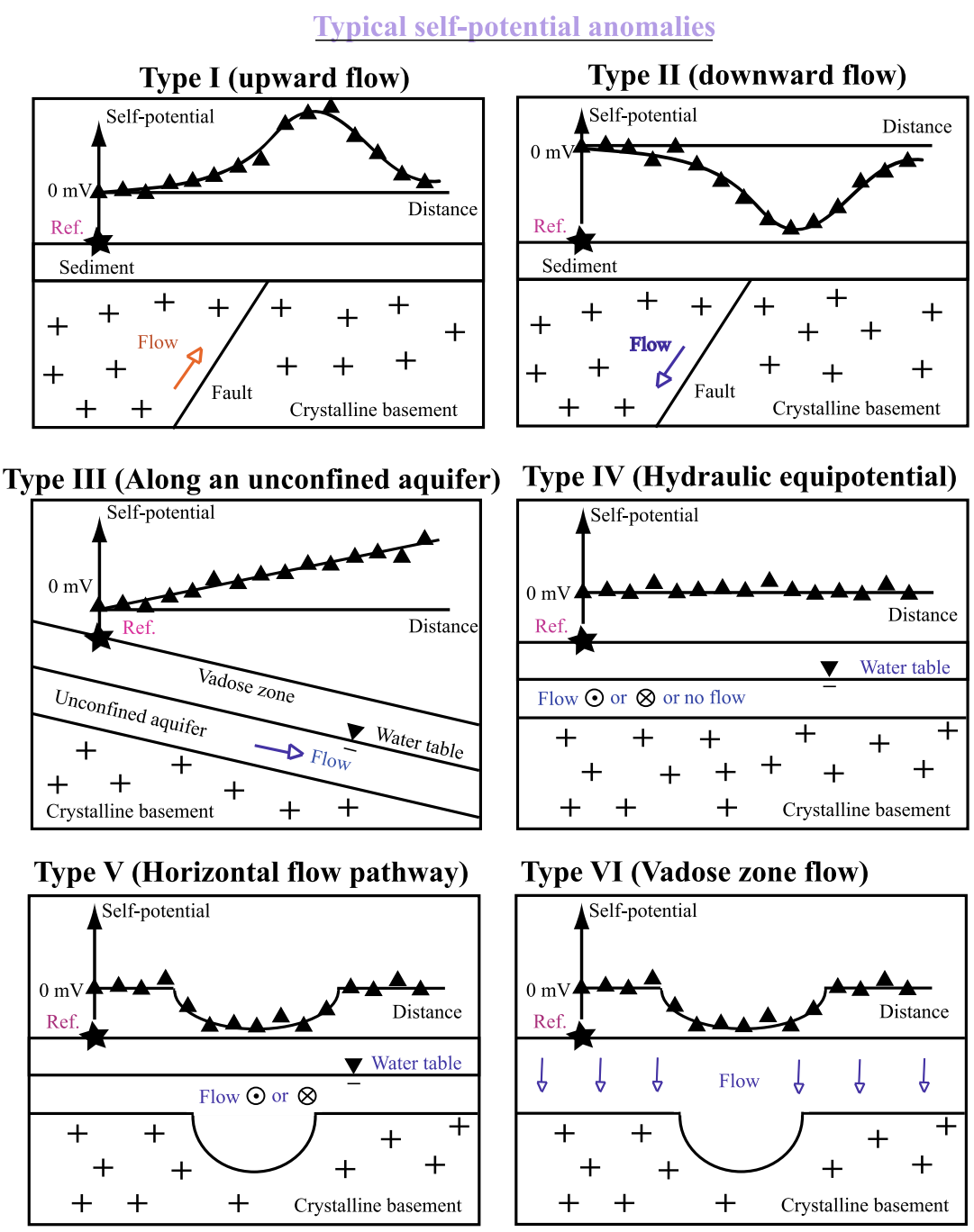

Fig. 11. Idealized self-potential distributions associated with simplified groundwater flow models. "Ref" denotes the position of the reference electrode. There are 6 types of anomalies sketched here and labeled Type I to VI. These anomalies are used to discuss field data all along the paper. Modified from Richards et al. (2013).

density and the streaming potential coupling coefficient C (in V Pa^{-1}) is given by

$$C = -\frac{\widehat{Q}_V(s_w)k(s_w)}{\sigma(s_w)\eta_w} \tag{8}$$

where σ denotes the DC (Direct Current) electrical conductivity of the porous material (in Ω m) and η_f (Pa s) the dynamic viscosity of the pore water. For pH comprised between 4 and 8, Jardani and Revil (2009a, 2009b) found that the excess charge density $\widehat{Q}_V$ (in C m^{-3}) can be related to the permeability k (in m^2) according to $log_{10}\widehat{Q}_V = -9.2 - 0.82log_{10}k$. It follows that the streaming potential coupling coefficient depends only weakly on the permeability itself. In order to solve the partial differential Eq. (6), we need to define the boundary conditions for the electrical potential, which are given by

$$\mathbf{E}\cdot\widehat{\mathbf{n}} = 0 \text{ on } \partial\Omega, \tag{9}$$

$$\varphi_\infty \rightarrow 0 \text{ in } \Omega, \tag{10}$$

where $\partial\Omega$ denotes the ground surface in contact with the atmosphere, $\widehat{\mathbf{n}}$ denotes the outward unit normal vector to this surface, and φ_∞ denotes the potential at infinity in the conductive ground Ω. In other words, the normal component of the electrical field to the ground surface vanishes at the ground surface and the potential is zero very far from the self-potential sources.

Because the excess of electrical charges is generally positive in the

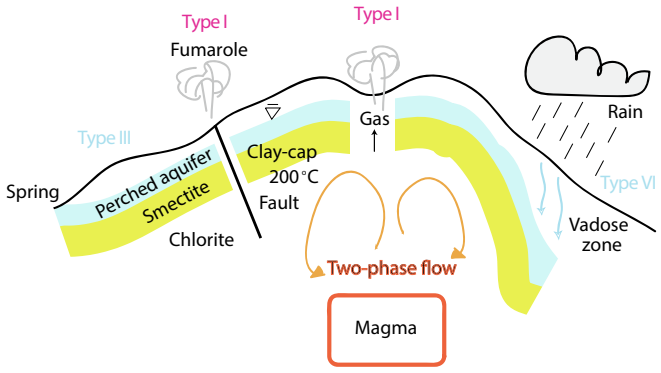

Fig. 12. Typical self-potential anomalies found on an active volcano. The upwelling of the groundwater flow in the hydrothermal system is associated with a positive self-potential anomaly at the ground surface (Type I). The upwelling of fluids along faults are also associated with positive anomalies (Type I). In the hydrogeologic zone, anomalies of Type III and VI are associated with perched unconfined aquifers and flow through the vadose zone, respectively.

pore water, the macroscopic (self- or electrical) potential is positive with respect to the direction of the groundwater flow (except for acidic pore waters as shown below). Figs. 11 and 12 show a series of sketch of the typical self-potential anomalies associated with groundwater flow in hydrothermal systems. These sketches are useful to provide a first idea of what to expect for typical and simple patterns of groundwater flow.

In order to be more quantitative, numerical codes have been developed to model self-potential signals associated to forward fluid flow simulations (e.g., Yasukawa et al., 1993; Bolève et al., 2007a, 2007b; Ishido and Pritchett, 1999; Titov et al., 2005; Alarouj et al., 2021a, 2021b; Arens et al., 2022). In subsurface hydrothermal reservoirs, numerical investigations have been able to successfully reproduce self-potential anomalies (e.g., Aizawa et al., 2009; Byrdina et al., 2013; Ishido, 2004; Onizawa et al., 2009; Revil, 2010; Yasukawa et al., 2003). We will discuss two cases in Section 5 to illustrate forward modeling approaches.

4.2. Forward modeling: dynamic hydromechanical problems

We consider briefly now the case a bit more general for which hydromechanical effects produced transient self-potential anomalies. By "hydromechanical", we mean any mechanical disturbance in which pore fluids play a role, for instance through the pore pressure. Pride (1994) volume-averaged the local Maxwell equations to obtain a set of macroscopic Maxwell equations in the thin-double layer limit (see also Revil and Linde, 2006, for the thick double layer case). Neglecting induction, the form of the four macroscopic Maxwell equations (Faraday's law of induction, Ampère's law, Gauss's law for magnetism, and Gauss's law for the electrical field) is given by,

$$\nabla \times \mathbf{E} \approx 0 \tag{11}$$

$$\nabla \times \mathbf{H} = \mathbf{j} + \dot{\mathbf{D}} \tag{12}$$

$$\nabla \cdot \mathbf{B} = 0 \tag{13}$$

$$\nabla \cdot \mathbf{D} \approx 0 \tag{14}$$

where $\mathbf{B} = \nabla \times \mathbf{A}$ denotes the magnetic field (in T), $\mathbf{A}$ (in T m) denotes the magnetic potential vector, $\mathbf{H}$ is the auxiliary magnetic field (in A m^{-1}), $\mathbf{D}$ is the current displacement vector (in C m^{-2}), and $\mathbf{E} = -\nabla\varphi - \dot{\mathbf{A}}$ the electrical field with φ denotes the electric (scalar) potential (in V). The quantity φ denotes the transient self-potential. These equations are completed by three constitutive equations:

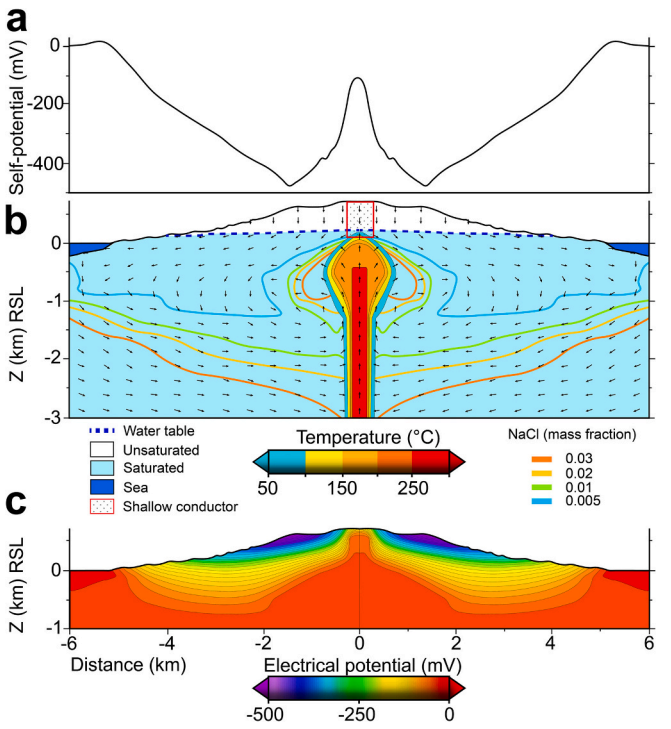

Fig. 13. Self-potential model of Izu-Oshima volcano (Japan) obtained after post-processing finite difference multiphase flow model (modified from Ishido, 2004). a. Modeled "W-shaped" self-potential anomaly. b. 2-D axisymmetric fluid flow model of the volcanic island. A deep heat source is imposed at 250 °C in the central zone, and is connected to the surface through a permeable conduit. Meteoric recharge is set at 400 mm per year. After 100 years of constant heat, the thermal structure shows a hydrothermal plume (50–250 °C) developed in the vicinity of the vertical conduit, and below the water table (blue dotted line). Black arrows indicate saline fluid circulation: high salt mass fraction (solid red line, NaCl = 0.03) highlights the seawater intrusion beneath the island, while less mineralized fluids (solid blue-green lines, NaCl≤0.005) are associated with meteoric infiltration. The upper red rectangle is a conductive region fixed at 1S m^{-1} in order to reproduce the amplitude of the central self-potential anomaly of +400 mV (Model G T-C from Ishido, 2004). c. Electrical potential distribution calculated from the post-processing of the multiphase flow result. The two lobes of negative electrical potentials visible on the volcano flank (−500–-300 mV) are induced by meteoric infiltration while the central positive anomaly results from a combination of fluid upwelling together with the presence of conductive rocks. (For interpretation of the references to colour in this figure legend, the reader is referred to the web version of this article.)

$$\mathbf{j} = \sigma\mathbf{E} + \widehat{Q}_V\dot{\mathbf{w}} \tag{15}$$

$$\mathbf{D} = \varepsilon\mathbf{E} \tag{16}$$

$$\mathbf{B} = \mu\mathbf{H} \tag{17}$$

where ε is the permittivity of the porous body and μ denotes its magnetic permeability. These equations are coupled to the hydromechanical equations via the current density. To be explicit, we consider the simple case of linear poroelasticity (like recently in Arens et al., 2020, 2022) but any rheology incorporating the pore space and its fluid pressure could be used to better handle the (thermo)-hydromechanical problem including poro-visco-plasticity. Two momentum conservation equations are needed and given by

$$\left(\frac{1}{M} + \frac{\partial\theta}{\partial p_w}\right)(p_a - p_w) = \frac{C}{M}\nabla\cdot\mathbf{u} + \nabla\cdot\mathbf{w} \tag{18}$$

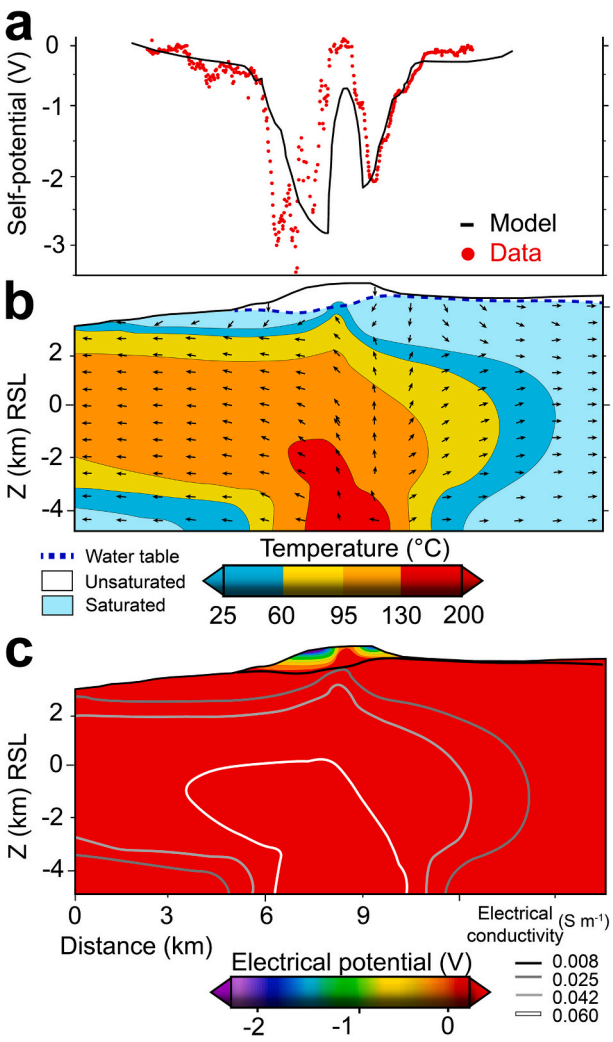

Fig. 14. Self-potential model of Ticsani volcano (Peru) obtained after post-processing finite element multiphase flow model (modified from Byrdina et al., 2013). a. Modeled "W-shaped" self-potential anomaly (black solid line) compared with real self-potential measurements (red points). b. 2-D axisymmetric fluid flow model of the volcanic island. A deep heat source is imposed at depth in the central zone, and is connected to the surface through a permeable conduit. Meteoric recharge is set at 150 mm per year, except above the central conduit region. After 30,000 years of constant heat, the thermal structure shows a hydrothermal plume (~50–200 °C) developed in the vicinity of the vertical conduit. Black arrows indicate fluid circulation, and blue dotted line represents the water table. c. Electrical potential distribution calculated from the post-processing of the multiphase flow results and its inferred conductivity structure (white-black lines). The two lobes of negative electrical potentials visible on the volcano flank (−2 V) are induced by meteoric infiltration while the central positive amplitude (+2 V) results from a combination of fluid upwelling and conductive rocks. (For interpretation of the references to colour in this figure legend, the reader is referred to the web version of this article.)

$$\nabla\cdot\overline{\overline{T}}+\mathbf{F}=\rho\ddot{\mathbf{u}}+\rho_f\ddot{\mathbf{w}} \tag{19}$$

where **u** and **w** are the averaged displacement of the solid phase and the average filtration displacement associated with the liquid water phase, respectively, M and C are two Biot coefficients, $\overline{\overline{T}}$ is the total stress tensor, **F** denotes the body force applied to the porous material (including the gravity force), $\theta=s_w\phi$ denotes the water content (dimensionless), ρ is the mass density of the material, and ρ_f is the mass density associated with the liquid water phase (product of the saturation by the density of the liquid water phase). In addition, we need the following Biot constitutive equation,

$$-p=C\nabla\cdot\mathbf{u}+M\nabla\cdot\mathbf{w} \tag{20}$$

where p denotes the liquid water pressure. The two mechanical moduli entering these equations are defined in unsaturated conditions as

$$\frac{1}{C}=\frac{1+\Delta}{K_f+K_S\Delta} \tag{21}$$

$$\frac{1}{M}=\theta\left(\frac{1+\Delta}{K_f}\right) \tag{22}$$

where the two quantities in Eqs. (21) and (22) are defined by

$$\Delta=\left(K_f/\phi K_S^2\right)\left[(1-\phi)K_S-K_{fr}\right] \tag{23}$$

$$\zeta=-\nabla\cdot\mathbf{w}=\theta(\nabla\cdot\mathbf{u}-\nabla\cdot\mathbf{u}_w) \tag{24}$$

The quantity ζ denotes the linearized increment of fluid content (dimensionless). The quantity $\alpha_w=s_w\left(1-K_{fr}/K_S\right)$ denotes the Biot coefficient in unsaturated conditions, K_f is the bulk modulus for the pore fluids (related to the bulk moduli of the gas and liquid water phase by Wood formula), K_S and K_{fr} denote the bulk moduli for the solid and skeleton, respectively. Solving together the semi-coupled hydromechanical and electromagnetic problems presented above can be used to assess the intensity of the electromagnetic disturbances associated with hydromechanical disturbances in a hydrothermal system. We will discuss an example in Section 5.7.

4.3. Inverse modeling

Initially, the development of source localization algorithms was developed with simple sources (charge accumulations) using error and trial approaches or cross-correlation algorithms (Corwin and Hoover, 1979; Patella, 1997a, 1997b). These methods are now considered outdated because they do not bring meaningful information regarding the causative sources, its geometry, and its connection to groundwater flow.

In the forward modeling approach described above, we can model the self-potential response associated with either steady-state groundwater flow or hydromechanical disturbances. For a given set of boundary conditions and distribution of the material properties, the solution of the forward modeling is always unique. The inverse problem consists in recording the self-potential data at the ground surface (possibly in boreholes) and invert this self-potential response to characterize the causative source (e.g., Long and Hao, 2005; Revil and Jardani, 2013), even possibly the pattern of groundwater flow itself or the localization of the hydromechanical disturbances (e.g., Haas et al., 2013). As mentioned above, the knowledge of the conductivity structure of the subsurface is an important ingredient of the self-potential inverse problem and can be determined by passive or active electromagnetic surveys or galvanometric resistivity surveys. In addition, it should be recognized upfront that the solution of potential field problem is strongly non-unique, i.e., there are many of current source distributions that would produce the same sampled self-potential pattern at the ground surface. There are so-called annihilators, i.e., source current distributions that produce no detectable self-potential anomalies at the observation points. The anomaly of type IV described in Fig. 11 is an example of annihilator.

All these points are well-established in the realm of geophysical inverse problems and especially in the inversion of potential field data (e.g., gravity or magnetic data). In addition, there is a vast literature in Electro-EncephaloGraphy (EEG) in which we can reuse many existing algorithms to characterize hydrothermal fields from self-potential anomalies (see Grech et al., 2008, for a review of the inverse problem in EEG). Indeed, brain activity generates tiny source current densities at the synapses between the neurons, which, in turn, are responsible for

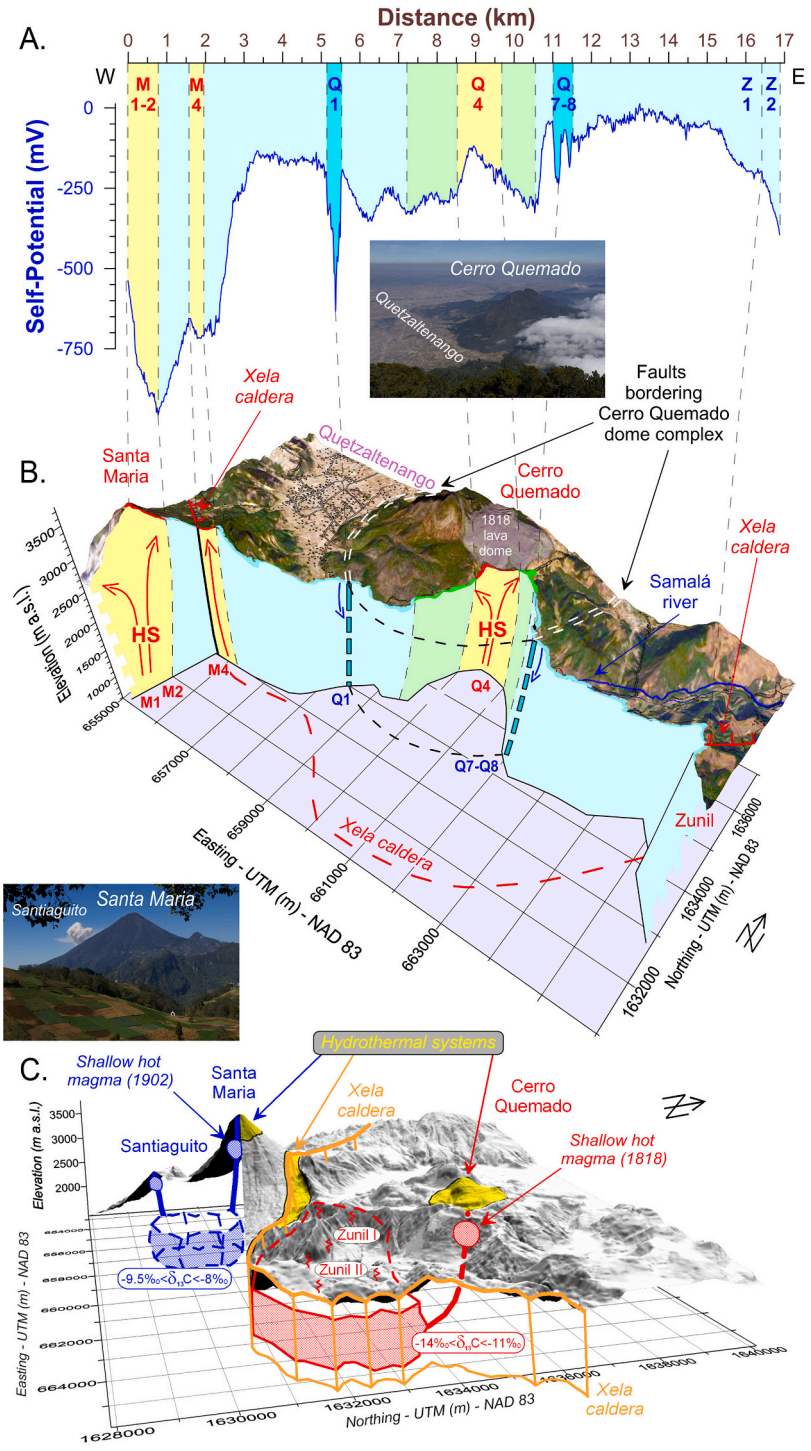

Fig. 15. Self-potential anomalies associated with the volcanic complex of Santa Maria – Cerro Quemado – Zunil volcanoes and Xela caldera. a. Self-potential over a ~ 17 km long profile. b. Interpretative 3D block of the self-potential signal. Letters correspond to the anomaly commented in the text. "HS" stands for hydrothermal system. c. Schematic 3D view of hydrothermal fluid flows consistent with self-potential data and isotopic gas geochemistry (modified from Bennati et al., 2011).

detectable self-potential signals on the scalp. These signals can be recorded with a network of electrodes applied to the scalp or using capacitive coupling technologies and used to monitor brain activity or to locate for instance the source of epilepsy.

In the approach we discuss now, the first step is to compute the Kernel matrix that represents the relationship between the electrical current density at source point M and the measured self-potential signals at a self-potential station P (observation point) for instance located at the ground surface. The relationship between the potential at P, $\varphi(P)$, and the current density at source position M, $\mathbf{j}_S(M)$, is given by the integral form of the Poisson equation, Eq. (6),

$$\phi(P) = \int_{\Omega} \mathbf{K}(P,M)\mathbf{j}_S(M)dV \tag{25}$$

where $\mathbf{K}(P,M)$ denotes the kernel, which incorporates the conductivity distribution if known. This matrix allows to compute the self-potential at

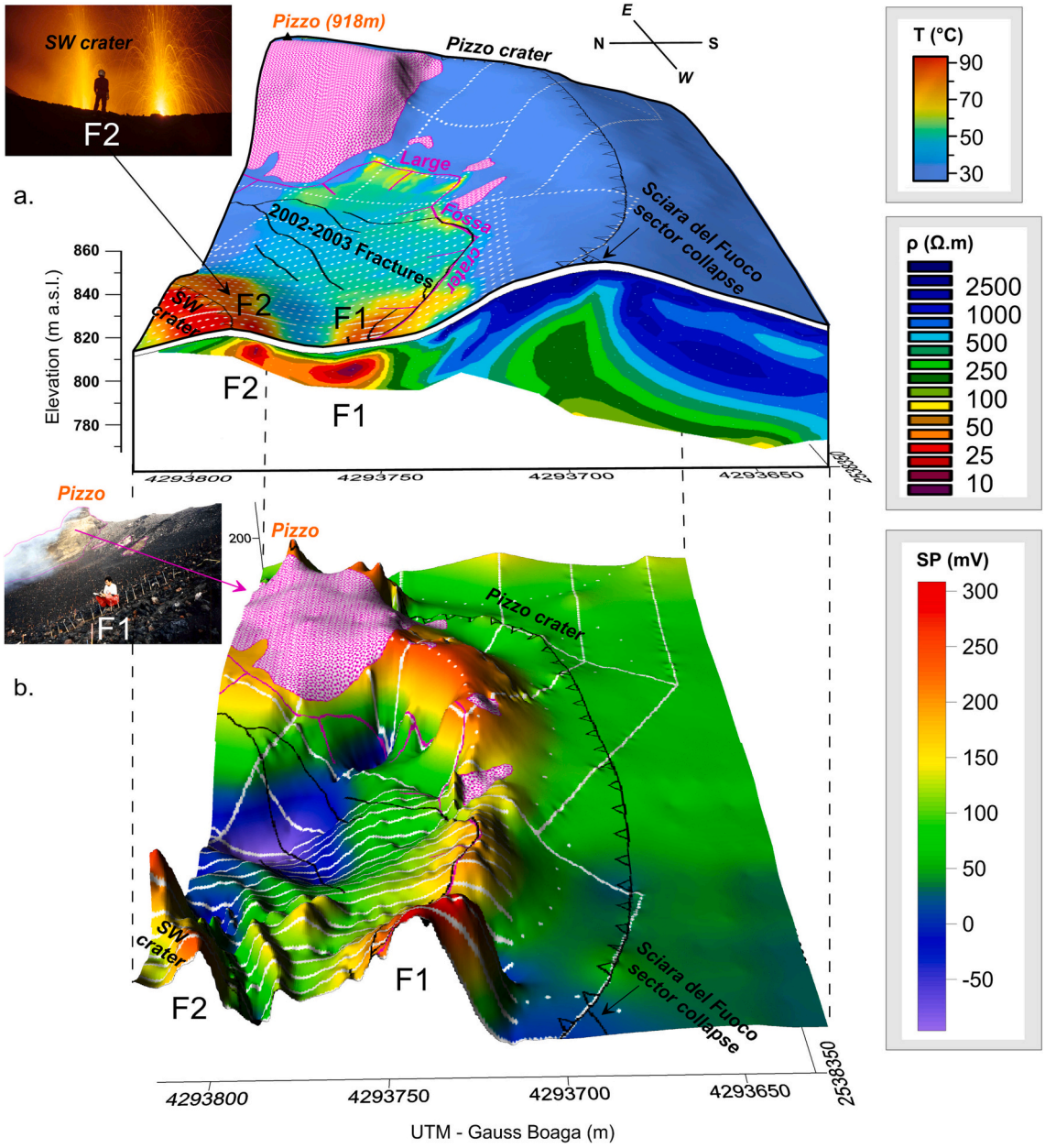

Fig. 16. Summit part of Stromboli volcano, Aeolian islands, Italy. White dots correspond to the self-potential measurements. Pink colour is used to delimitthe Pizzo pyroclastic outcrop where no data can be taken a. 3D view showing temperature measurements taken at 30 cm depth on (X-Y) plane and electrical resistivity tomography on (X-Z) plane (ρ the resistivity in Ohm m). b. Self-potential map visualized in 3D view (modified from Finizola et al., 2009). (For interpretation of the references to colour in this figure legend, the reader is referred to the web version of this article.)

point P for an elementary current source vector located at the source point M in the ground Ω characterized by a non-uniform electrical conductivity distribution. Therefore, the size of the kernel matrix depends on the number of measurement stations N and the number M of elements used to discretize the ground. In essence, each element of this matrix is a Green function that can be numerically computed to account for the electrical conductivity distribution, the boundary conditions (Eqs. (9) and (10)), and the topography. Finally, when computing numerically the elements of $\mathbf{K}$, one has to remember that the electrical potential is determined relative to a reference electrode located somewhere at the ground surface (see Section 3.2 above). As explained above, this choice is arbitrary but needs to be consistent between the display of the data and the numerical forward modeling used to compute the kernel (see Jardani et al., 2008, for details). This is a crucial step in order to compare field data and modeled data and it should not be forgotten.

There are many ways to invert self-potential data. The simplest is to envision the inversion of the self-potential inversion in two steps. In the first step, the measured self-potential field is inverted to determine the source current density distribution. In the second step, this source current density distribution is converted into a distribution of the Darcy velocity $\dot{\mathbf{w}}$ using the distribution of $\mathbf{j}_S$ and assuming reasonable values for the volumetric charge density $\widehat{Q}_V$. One key-question is to incorporate prior knowledge of the flow field (and therefore the source current density) in order to guide the inversion toward a meaningful hydrogeological model.

Regarding the first step, the self-potential inverse problem is a typical potential field problem and the solution of such problem is ill-posed and non-unique. It is therefore important to add constraints to reduce the solution space for the current density distribution. Using the L_2 norm assuming Gaussian probability densities on the data and model

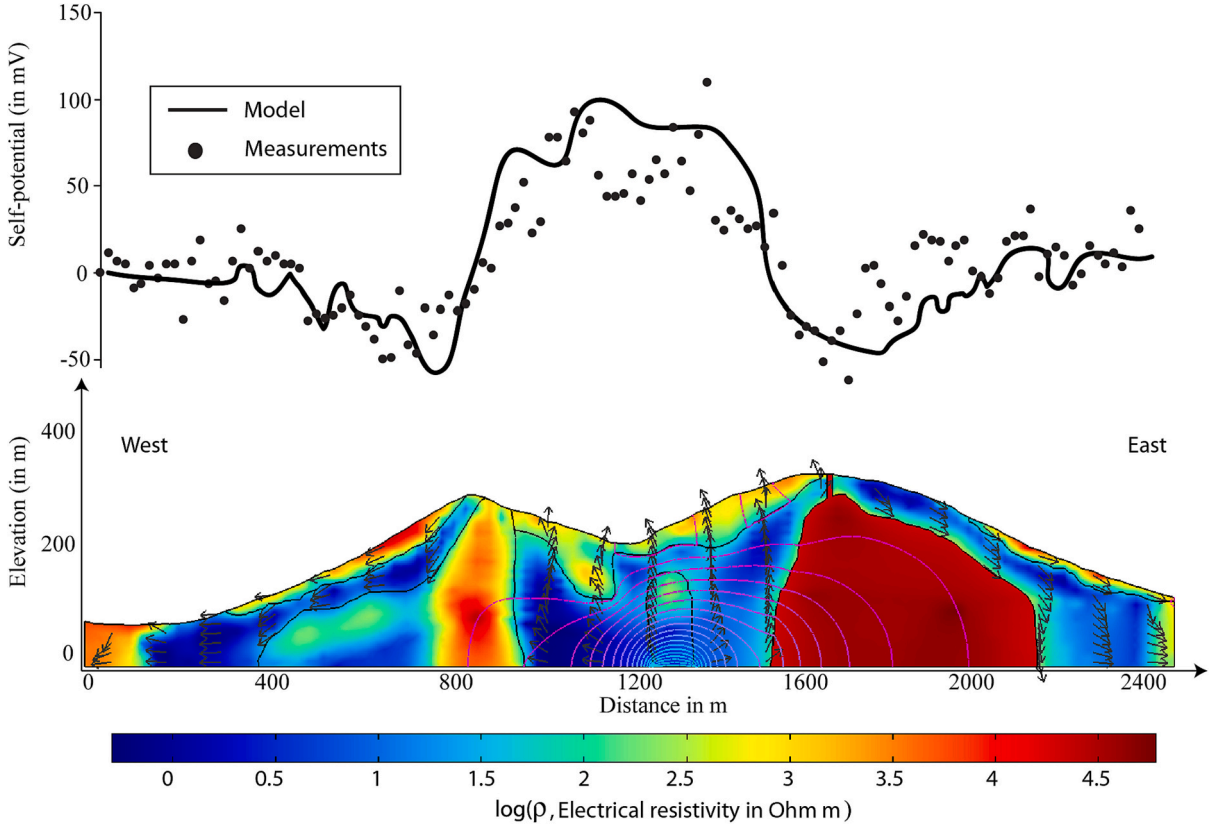

Fig. 17. Ground-water flow model obtained by inverting the self-potential data measured at the ground surface. The positive self-potential anomaly in the center of the volcano is associated with the upwelling of the hot water (Type I anomaly) while the flanks of the volcano are associated with Type III anomalies associated with groundwater flow in shallow aquifers. We use first the resistivity data and the self-potential data to invert the source current density distribution under constraints. Then this source current density distribution is converted into a normalized Darcy-velocity distribution. Modified from Revil et al. (2008).

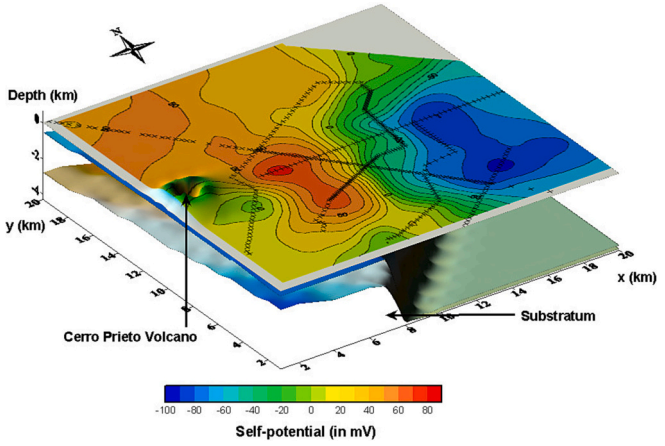

Fig. 18. Self-potential map measured at the ground surface of the Cerro Prieto geothermal field using the data from Fitterman and Corwin (1982, see also Revil and Pezard, 1998). The crosses materialize the self-potential stations. The dipolar anomaly exhibits a peak-to-peak amplitude of 160 mV, which is not a strong anomaly by comparison with those exhibited in Figs. 1 to 3. The position of the substratum basement is determined from well data combined with geophysical surveys. Modified from Jardani et al. (2008). The positive anomaly reflects the upflow of hot water.

probability functions and no prior model, a model objective function $\psi_\lambda(\mathbf{m})$ is written to balance the data misfit function and constrain function using Tikhonov regularization,

$$\psi_\lambda(\mathbf{m}) = \|\mathbf{W}_d(\mathbf{Km} - \varphi_d)\|^2 + \lambda\|\mathbf{W}_m\mathbf{m}\|^2 \tag{26}$$

In this equation, λ corresponds to the (unknown) parameter (with $0 < \lambda < \infty$) that balances the two components of the cost function (i.e., data misfit and the regularization terms). We use the definition $\|\mathbf{Af}\|^2 = \mathbf{f}^t\mathbf{A}^t\mathbf{Af}$ where t denotes transpose. The kernel $\mathbf{K} = \left(\mathbf{K}_{ij}^x, \mathbf{K}_{ij}^y, \mathbf{K}_{ij}^z\right)$ ($N \times 3M$)-matrix comprises three elements for each of the three directions of the Cartesian coordinate system. The quantity $\mathbf{Km}$ represents the simulated self-potential data given a 3 M-model vector $\mathbf{m} = \left(j_i^x, j_i^y, j_i^z\right)$ describing the source current density at each cell used to discretize the subsurface (M cells in total). The vector φ_d corresponds to the N-measured self-potential data. The $N \times N$-matrix $\mathbf{W}_d = diag\{1/\varepsilon_1, \ldots, 1/\varepsilon_N\}$ is used to weight the data according to the level of error (ε_i denotes the standard deviation of the self-potential measurement i). The 2 (M-2) $\times$ 2 M matrix $\mathbf{W}_m$ denotes the flatness matrix or the differential Laplacian operator. A Gaussian assumption on the data is used to set up the matrix $\mathbf{W}_d$, which is a diagonal matrix based on the data covariances. For the matrix $\mathbf{W}_m$, we use the smoothness operator (the discrete approximation of the second order derivative) and therefore roughness of the solution (in terms of current density distribution) is penalized.

We can also start the inversion with a prior model based on groundwater flow that we can perturb using the self-potential data. In the case where a prior model $\mathbf{m}_0$ would be considered, $\|\mathbf{W}_m\mathbf{m}\|^2$ would be replaced by $\|\mathbf{W}_m(\mathbf{m} - \mathbf{m}_0)\|^2$ in eq. (26) to account for this model.

The best model is obtained by minimizing $\psi_\lambda(\mathbf{m})$ (i.e., looking for $\partial\psi_\lambda(\mathbf{m})/\partial\mathbf{m} = 0$. The model update vector $\Delta\mathbf{m_i}$ is given by using the Gauss-Newton technique. The value of λ can be optimized using the L-curve technique or can be decreased step by step at each iteration to fit the self-potential data at its level of noise (cooling approach).

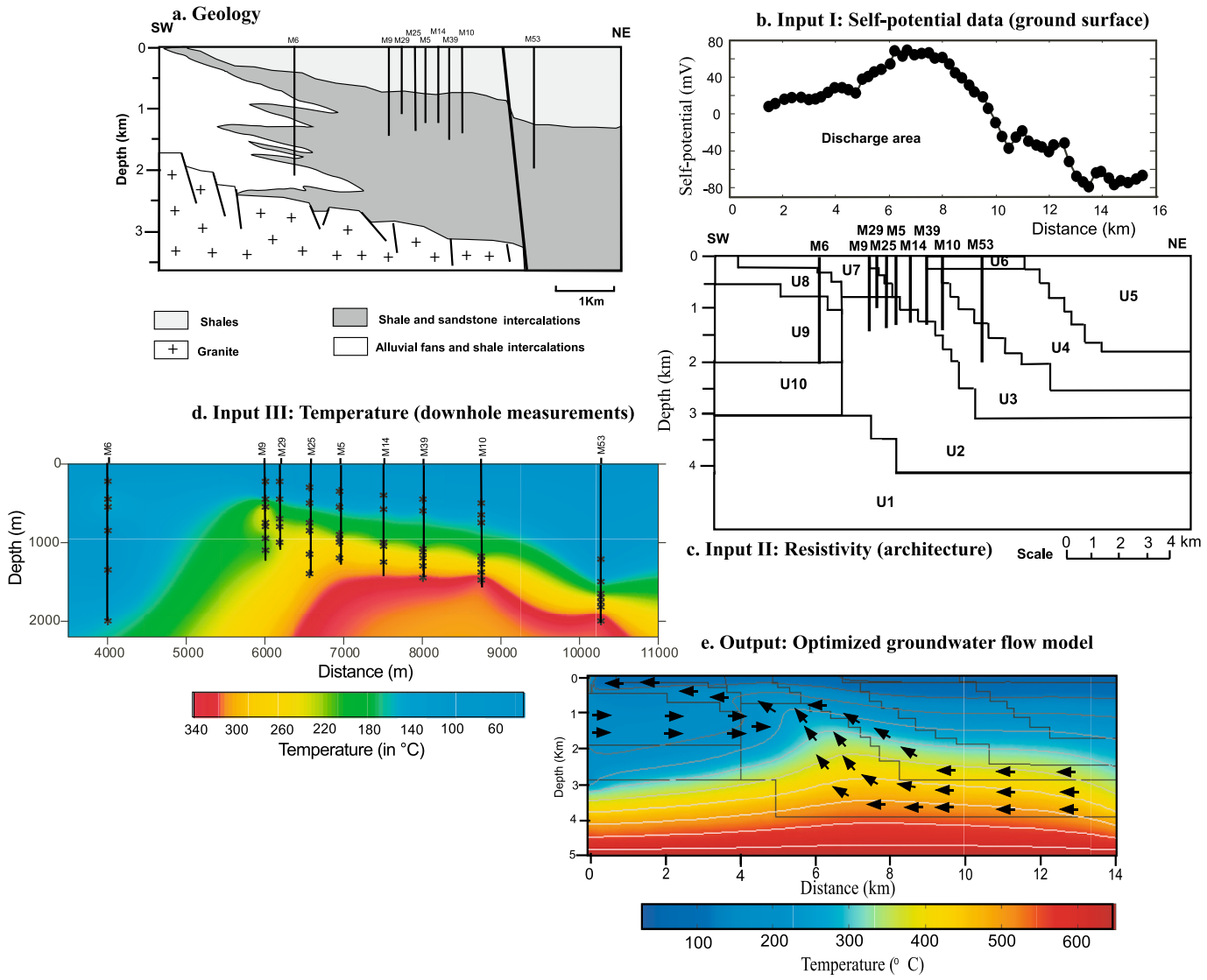

Fig. 19. Result of the inversion of the self-potential field measured at the Cerro Prieto geothermal field in Mexico in the vicinity of the Cerro Prieto volcano. a. Sketch showing the geology below the self-potential profile. b. Self-potential profile (data obtained from the study of Corwin et al., 1979). "Ref" denotes the position of the reference electrode. c. Electrical resistivity tomogram using vintage apparent resistivity data. The resistivity tomogram is used to define the main lithological units used to define the hydrogeological model. d. Temperature field using extrapolated well temperature data. e. Result of the stochastic inverse modeling used to invert the hydrogeological parameters needed to determine the groundwater flow model. Modified from Jardani and Revil (2009).

5. Applications

In this section, we discuss several case studies to highlight forward and inverse modeling procedures and results. Forward numerical modeling is discussed in Section 5.1. The acquisition and analysis of field data is performed in Sections 5.2 and 5.3 for Peruvian, Guatemalan, and Italian volcanoes. Forward modeling of the self-potential signals from groundwater flow modeling is discussed in Section 5.4. Inverse modeling of self-potential signals in terms of groundwater flow pattern is discussed in Sections 5.5 and 5.6. In Section 5.7, we discuss self-potential anomalies associated with the ascent of acidic groundwaters in stratovolcanoes. A laboratory test associated with the upwelling of a hydromechanical disturbance is discussed in Section 5.8 where we also discuss transient self-potential data at La Fournaise volcan (Réunion island, France).

5.1. Forward modeling cases

Numerical codes have been developed in the literature to calculate self-potential signals associated with various forward steady state fluid flow simulations (e.g., Yasukawa et al., 1993; Ishido et al., 1997, Ishido and Pritchett, 1999; Titov et al., 2005; Bolève et al., 2007a, 2007b; Onizawa et al., 2009, Aizawa et al., 2009, Matsushima et al., 2017, Alarouj et al., 2021a, 2021b). Three main steps are necessary to forward-model the self-potential distribution:

(i) The definition of the conceptual model. Data of interest comprise: groundwater recharge and springs, thermal budget and degassing activity, geologic/tectonic features, petrophysical rock properties, and subsoil/subsurface interpreted geophysical tomograms.
(ii) The construction of the forward fluid flow model. This second step includes the selection of the equation of state, and the creation of the computational domain with initial rock properties and boundary conditions.
(iii) The post-processing of the resulting fluid flow structure to retrieve the electrical potential field. In this final step, the electrical conductivity distribution of the fluid flow model can be

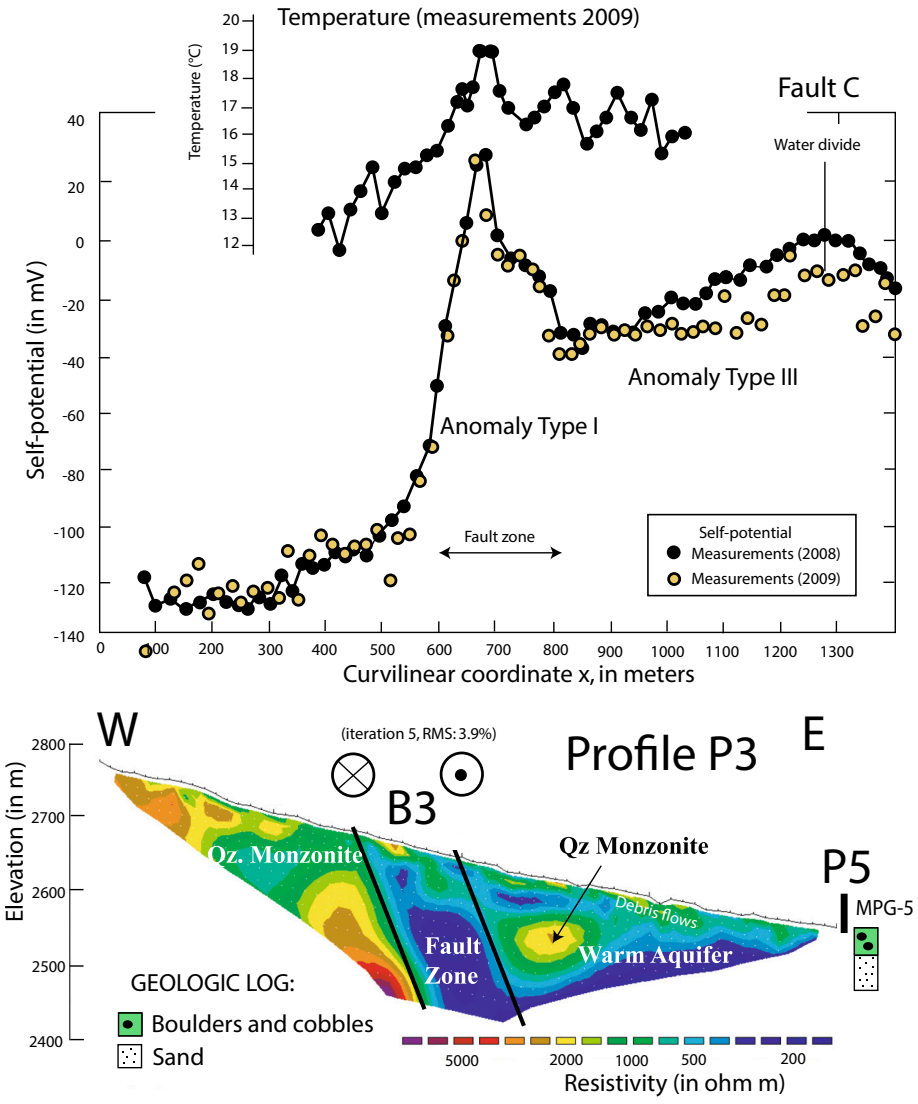

Fig. 20. Self-potential profile associated with the flow of the groundwater upwelling along a shear fault (Upper Arkansas Valley, Colorado, USA) crossing the batholith of a former volcano. The resistivity tomogram shows the position of the fault and the shallow aquifer. The positive self-potential anomaly of 150 mV is associated with the upwelling of the hot water in the fault plane (Type I anomaly). Further downslope, we can observe a self-potential anomaly of Type III. The arrows ⊗ and ⊙ represent the displacement of the shear fault. Modified from Richards et al. (2013).

calculated using empirical relationship in porous rocks (e.g., Revil and Gresse, 2021).

This approach has been used by various researchers to model the self-potential anomalies of volcanoes and geothermal systems, allowing the validation/confirmation of associated physical processes (e.g., Aizawa et al., 2009; Byrdina et al., 2013; Ishido, 2004; Onizawa et al., 2009; Matsushima et al., 2017; Revil et al., 2010a; Yasukawa et al., 2003). In order to illustrate this point, we summarize below the works of Ishido (2004) and Byrdina et al. (2013) who investigated the nature of the "W-shaped" self-potential anomalies on active volcanoes (Figs. 13 and 14). Both studies are based on groundwater flow simulations with a realistic conceptual model. Various rock properties values were used, for instance accounting for a reduction of the permeability with depth. A permeable vertical conduit was placed between the crater floor and a magmatic heat source at depth. The atmospheric boundary conditions were fixed including ground surface temperature, atmospheric pressure, air saturation, and meteoric recharge. The lateral boundary conditions were set to hydrostatic pressure in both simulations. It corresponds to an open convective flow in the study of Byrdina et al. (2013). The lateral boundary condition is closed to groundwater flow in the study by Ishido (2004). Furthermore, Ishido (2004) accounts for ocean boundary conditions (i.e., seawater intrusion) since this study focused on volcanic islands.

Forward fluid flow results show two similar features: (i) downward infiltration of meteoric water within the unsaturated zone, and (ii) hot hydrothermal plume lying above the deep magmatic source. The variation in the plume extent is controlled by different boundary conditions and permeability fields. Indeed, Ishido (2004) considered high rocks permeability (10^{-13}–10^{-14} m^2) enhancing convective heat transfer, while Byrdina et al. (2013) used instead lower permeability values (10^{-14}–10^{-15} m^2) promoting heat conduction with respect to free convection (low Rayleigh numbers).

The post-processing of the two fluid flow models successfully reproduced the measured self-potential signals observed at Ticsani and Izu-Oshima volcanoes both in terms of amplitude and shape (see Figs. 13 and 14). The two negative lobes of the "W-shaped" signal are generated by meteoric water infiltration within the unsaturated zone associated with low conductive materials (10^{-2}–10^{-5} $S{\cdot}m^{-1}$). The central positive self-potential anomaly is identified as the combination of hot fluid upwelling and shallow conductive materials (10^{-2}–10^{1} $S{\cdot}m^{-1}$). On volcanoes, the relative contributions of these two sources of electric potential depends on their inherited structure, past and recent activity (e.g., open/closed plumbing system, presence of clay cap). Monitoring of the large scale self-potential anomalies on active volcanoes could open the door to a powerful method to investigate their plumbing systems.

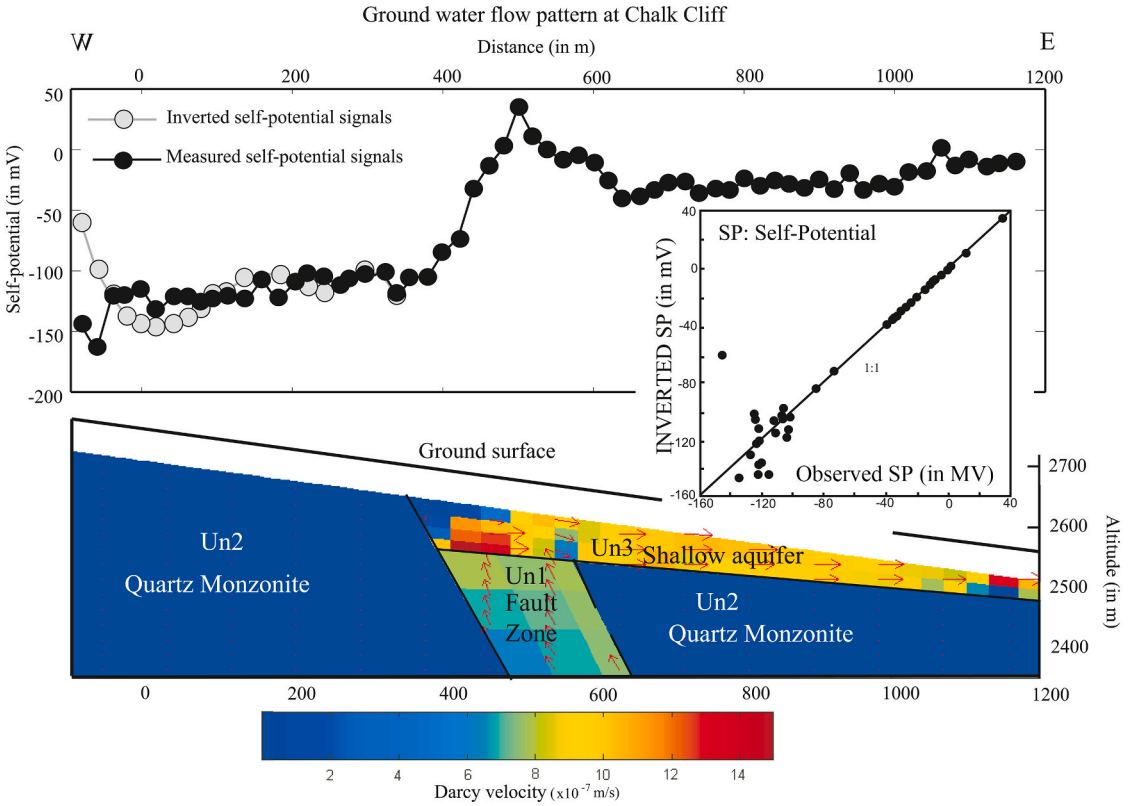

Fig. 21. Inversion of the self-potential signals in terms of current source distribution converted in groundwater flow pattern. Unit U1 corresponds to the open (pervasive) fault zone. Unit U2 represents the impervious quartz monzonite basement (the batholith of a former volcano). Unit U3 represents the shallow aquifer. The arrows and the colors along the flow path represent the direction and the amplitude of the Darcy velocity, respectively. The Darcy velocity is obtained by converting the source current density into Darcy velocity using the effective mobile charge density in the pore water. The insert shows the measured self-potential data versus those resulting from the optimized groundwater flow model (with a root mean square RMS error of 1.2%). Modified from Richards et al. (2013).

5.2. Large-scale study on Peruvian and Guatemalan volcanoes

The large-scale surveys performed on active Peruvian volcanoes, such as Misti (Finizola et al., 2004, see Fig. 1) and Ubinas volcanoes (Gonzales et al., 2014) revealed large amplitude self-potential anomalies with a classical "W" shape underlying a huge hydrothermal system several kilometers in diameter. Such a signal means the presence at a depth of few kilometers of a magmatic body (see Revil et al., 1999b for a description of the numerical modeling case study).

The density of active volcanoes in Guatemala implies particular strategy to study with self-potential, volcanic complexes such as the Santa Maria - Cerro Quemado - Zunil and Xela caldera (Bennati et al., 2011; see Fig. 15). A unique self-potential profile of about 17 km long, with a step of 20 m, have been performed, beginning at the top of Santa Maria volcano, crossing Xela caldera boundary, then following with the Cerro Quemado dome complex, and crossing again the Xela caldera boundary in direction to Zunil volcano.

The hydrothermal system of Santa Maria volcano is revealed by a positive self-potential / elevation gradient (anomalies M1-M2 in Fig. 15a and b) and the Western flank of Xela caldera boundary also facilitate the uprising of hydrothermal fluids, as attested by the positive self-potential / elevation gradient (M4 in Fig. 15a and b). A similar hydrothermal system appears close to the 1818 lava dome (anomaly Q4 in Fig. 15a and b). Around the Cerro Quemado dome complex, the presence of negative self-potential anomalies indicates the possibility of preferential groundwater infiltration along the faults bordering the Cerro Quemado dome complex (see anomalies Q1, Q7 and Q8 in Fig. 15a and b). This survey highlights the notion of partitioned hydrothermal systems on a volcanic complex, notion attested by the isotopic gas geochemistry (Fig. 15c).

5.3. Small-scale study in the summit part of Stromboli volcano

A high resolution survey (1 m spacing along profiles for self-potential and 2.5 m spacing for temperature recorded at a depth of 30 cm) was performed in 1999 in the summit area of Stromboli volcano (Finizola et al., 2003). Revil et al. (2004) performed an electrical resistivity tomography with 5 m spacing between the electrodes. An eruptive crisis occurred in 2002–2003, which opened fractures in the summit area (Finizola et al., 2009; see Fig. 16). It is interesting to note the strong correlation between the positive anomalies of self-potential, the temperature anomalies at a depth of 30 cm and the conductive bodies shown on the resistivity profiles (see anomalies F1 and F2 shown in Fig. 16). The superimposition between the 2002–2003 opened fractures and the maximum of the self-potential anomaly (F1 in Fig. 16) highlights that self-potential signals can be useful to anticipate weakness planes in the structure on a volcanic edifice, which can be reactivated during an unrest period. Similar observations were made by Chaput et al. (2019) before the collapse of the Dolomieu caldera on Piton de la Fournaise volcano at Réunion Island in the Indian Ocean.

5.4. Groundwater flow pattern at Vulcano (Italy)

La Fossa cone is an active stratovolcano located on Vulcano Island in the Aeolian Archipelago in the Mediterranean Sea (southern Italy). It self-potential anomaly (Fig. 17) exhibits a W-shape as those shown in Figs. 3, 13, and 14. A 3D resistivity tomogram was obtained by Revil et al. (2010b). The hydrothermal system is identified by very low values of the electrical resistivity (<20 Ohm m). Its lateral extension is clearly limited by the crater boundaries, which are relatively resistive (>400 Ohm m). Inside the crater it is possible to follow the plumbing system of

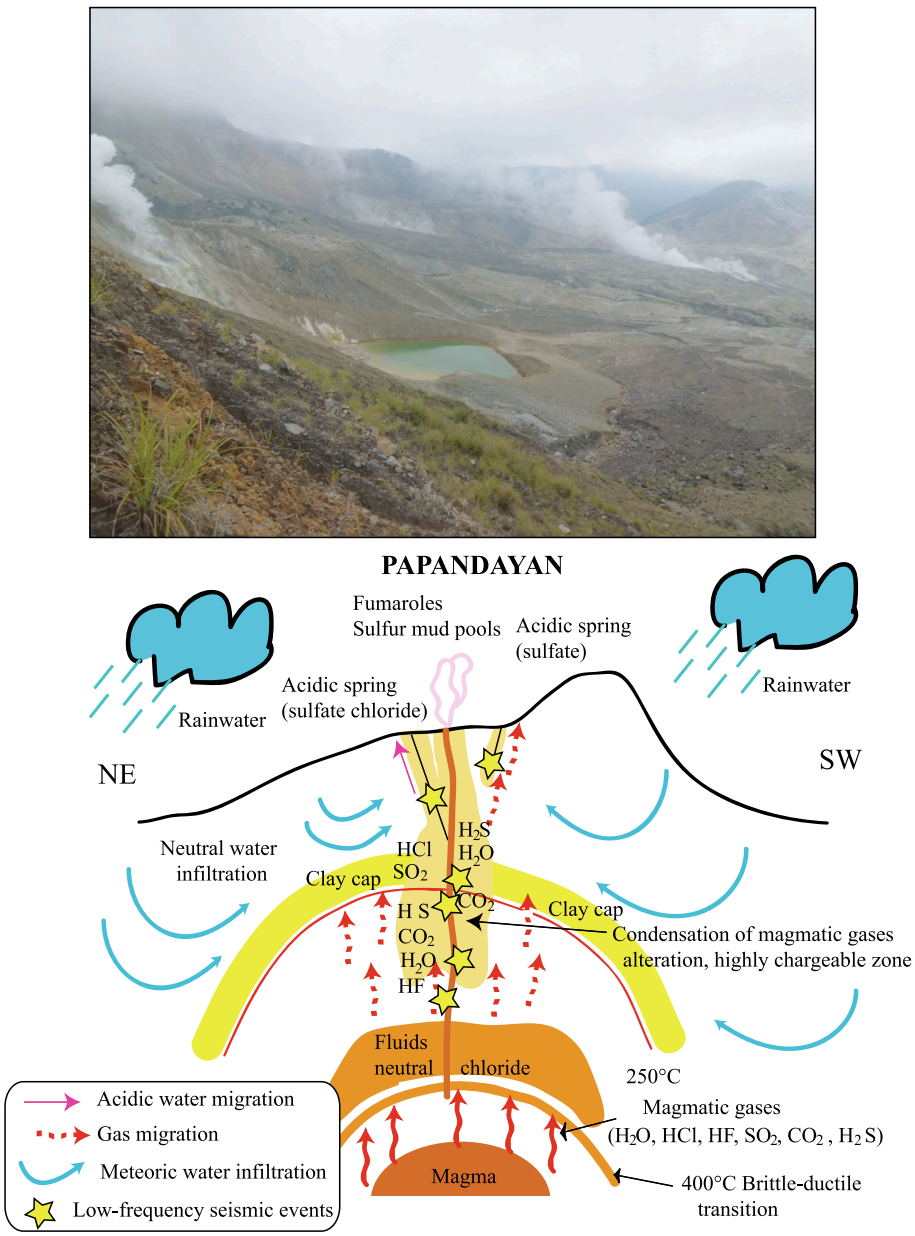

Fig. 22. Sketch showing the upwelling of acidic groundwaters in a stratovolcano (here Papandayan volcano in Indonesia, modified from Mazot et al., 2008). The stars correspond to the low-frequency seismic events. The clay cap is rich in smectite while the altered area around the acidic conduits is rich in kaolinite.

the main fumarolic areas. On the flank of the edifice a thick layer of tuff is also marked by very low resistivity values (in the range of 1–20 Ohm m) because of its composition in clays and zeolites.

A 2-D simulation of the groundwater flow is performed over the edifice using a commercial finite element code (Fig. 17). Input parameters are the topography, the conductivity cross section, and the value of the measured streaming current coupling coefficient on a set of core samples from the volcano. From this forward simulation we computed the self-potential field, and we found good agreement with the measured self-potential data by adjusting the boundary conditions for the flux of water (see Fig. 17 and see Revil et al., 2008, for details). Inverse modeling shows that self-potential data can be used to determine the pattern of groundwater flow and potentially to assess water budget at the scale of the volcanic edifice. The distribution of the current density can be then translated into a distribution of Darcy velocity, which can be integrated to determine the amount of water upwelling through the central part of the volcano. Two examples of such integration are shown in the next two sections.

5.5. *Inverse modeling: the case of Cerro Prieto (Baja California)*

We discuss now the interpretation of the 160 mV self-potential anomaly observed at the geothermal field of Cerro Prieto, Baja California, Mexico (Fig. 18). Inversion of the self-potential and resistivity data allows observing a plume of hot groundwater rising to the ground surface in the central part of the investigated area and discharging to the ground surface in the southwest part. The temperature anomaly associated with the existence of this plume is independently observed by interpolating borehole temperature measurements (Fig. 19). The analysis shown in Fig. 19 summarizes the results obtained by Jardani and Revil (2009a, 2009b) using a stochastic approach.

In hydrothermal fields, the flow of the groundwater is responsible for

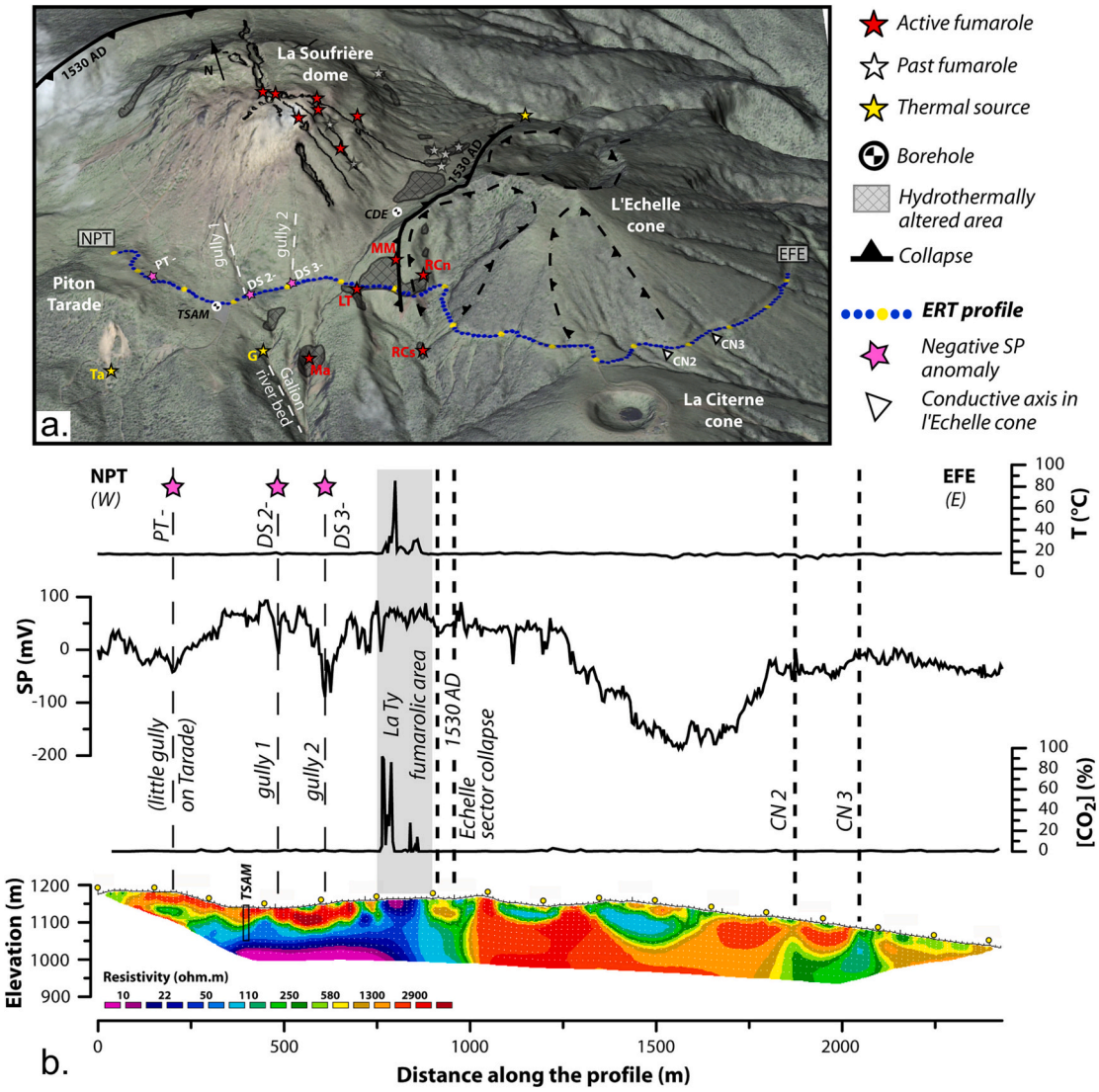

Fig. 23. Soufrière of Guadeloupe. a. Location of the multi-method profile on a 3D view with a satellite image superimposed on a digital elevation model of Soufrière of Guadeloupe. b. Temperature at 30 cm depth (°C), self-potential (mV), soil CO_2 concentration at 30 cm depth (ppm) measurements and electrical resistivity tomography along the profile. Yellow points on the tomogram correspond to benchmarks located each 150 m on the digital elevation model. Pink stars with PT-, DS2- and DS3- represent the negative self-potential anomalies. Note the light grey colour rectangle underlying the main hydrothermal rising fluid area (high temperature, high soil degassing and electrically conductive anomalies) but with no significant self-potential anomalies. "PT" and "DS" stand for Piton Tarade and Dome South respectively. CN stands for Conductive axis. TSAM and CDE correspond to boreholes. "NPT" and "EFE" means North of Piton Tarade and Eastern flank of l'Echelle cone respectively (Modified from Brothelande et al., 2014). (For interpretation of the references to colour in this figure legend, the reader is referred to the web version of this article.)

both thermal and self-potential anomalies. Temperature is usually recorded in boreholes while the self-potential field is recorded at the ground surface (Fig. 18). As discussed by Jardani and Revil (2009a, 2009b), the joint inversion of temperature and self-potential data represents therefore an attractive approach to invert the flow field and permeability. Jardani and Revil (2009a, 2009b) used an Adaptive Metropolis Algorithm to determine the posterior probability densities of the material properties of different geological formations and faults by inverting jointly self-potential and temperature data. Their algorithm was first successfully tested using a synthetic case corresponding to a series of sedimentary layers overlying a low-permeability granitic substratum. Then an application to the Cerro Prieto data was also performed. The upwelling of a hydrothermal plume through a set of faults and permeable formations at the Cerro Prieto geothermal field in Baja California explains both the observed self-potential and thermal anomalies (Fig. 19). The optimized permeability values are in close agreement with independent hydrogeological estimates. The stochastic approach developed by Jardani and Revil (2009a) appears therefore as a noninvasive method for remote detection and three-dimensional mapping of subsurface groundwater flow in hydrothermal fields.

5.6. *Upflow of thermal water along a shear fault (Colorado)*

We move now to a case study in the upper Arkansas Valley in Colorado, at the feet of Mount Princeton, which is part of the Collegial Peaks. Mount Princeton is the batholith of a former volcano and is composed of quartz monzonite. The Mount Princeton hot springs is partly associated with the upflow of thermal water along a major crustal shear fault. Such crustal faults are often associated with volcanism. The self-potential anomaly and shallow resistivity structure associated with an open conduit along this shear fault is shown in Fig. 20. Our goal here is to show how we can quantify the flux of thermal water upwelling along the open conduit of the fault using the self-potential anomaly (see Richards et al., 2010, for details).

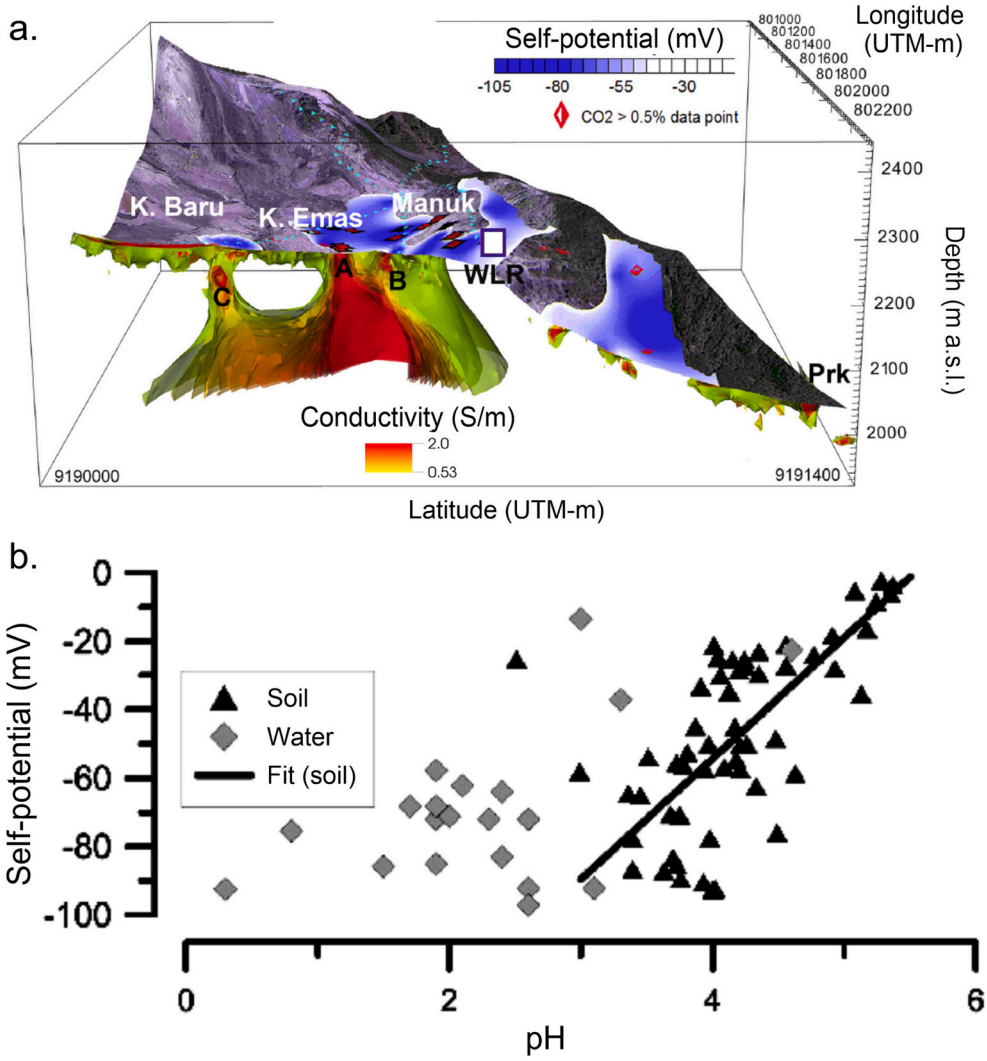

Fig. 24. Papandayan volcano. a. Satellite image superimposed on the digital elevation model of Papandayan volcano with representation of self-potential map below -40 mV and 3D representation of the most conductive areas (above 0.5 S/m) "A", "B", "C" associated with the three main fumarole field, K. Emas, Manuk and K. Baru respectively. WLR represents the permanent seismic station and Prk correspond to the parking area. b. Relationship between self-potential and pH measurements performed in soil (blach triangles) and pH measurements performed in water (grey diamonds) (Modified from Byrdina et al., 2018).

In order to quantify the flux of hot water, we use the geometrical model shown in Fig. 21 with the resistivity values obtained from the resistivity tomogram shown in Fig. 20. The geometry of the 2D model is simplified in three units. Unit U1 corresponds to the fault itself. Unit U2 represents the quartz monzonite basement (mostly impervious) while U3 denotes the shallow aquifer (made of granular sandy materials). The presence of this shallow aquifer is confirmed by a drill-hole (labeled MPG-5). The presence of hot water (at a temperature of 59 °C) was observed in Well MPG-5 at a depth of 40 m. The pH of the hot springs at Mount Princeton is comprised between 7.8 and 8.6 and therefore eq. (8) can be used to model the relationship between the excess of charge per unit pore volume $\widehat{Q}_V$ and the permeability k.

The boundary conditions used to simulate the steady-state groundwater flow and the associated self-potential problems are (i) impervious boundaries except at the base of the fault and at the outflow of the aquifer and (ii) insulating boundaries at all the external boundaries. The self-potential measurements shown in Fig. 20 were inverted to determine the magnitude of the Darcy velocity using the deterministic approach discussed in Section 4.3. A constant value for $\widehat{Q}_V$ inside U1 is used. Using a depth of the reservoir of 5 km and a mean geothermal gradient of 28 °C km^{-1} (measure independently in the area), the permeability of the fault plane is estimated to be on the order of 10^{-13} m^2. This yields an approximate value of $\widehat{Q}_V = 30\text{C m}^{-3}$ using eq. (8). The conductivity of the hydrothermal water is σ_w (25 °C) = 0.048 S/ m (measured in the Well MPG-5) close to the fault.

In order to produce a reasonable hydrogeological model, we use the additional conditions on the direction and magnitude of the source current density in each unit: $\mathbf{m} = \left(j_i^x \leq 0, j_i^z \approx 0\right)$ in U3 (i.e., flow is mainly horizontal in the shallow aquifer), $\mathbf{m} = \left(j_i^x < j_i^z\right)$ in U1 (i.e., flow is mostly vertical along the fault), and $\mathbf{m} = (0, 0)$ in unit U2 (no flow in the granitic basement). The minimization of the cost function corresponding to eq. (26) is performed iteratively by the Gauss-Newton method described in Section 4.3. The value of the regularization parameter is based on the level of noise in the self-potential data. We invert the current density distribution. Then this current density distribution is translated into a Darcy velocity distribution using eq. (4) and the value of $\widehat{Q}_V$ obtained above. Then the Darcy velocity can be integrated along the dimension of the fault characterized by the positive self-potential anomaly. This yields an integrated flux of 4000 m^3/day of hot water at 85 °C (see Richards et al., 2010, for details). A similar approach was followed recently by Miller et al. (2018) for Mount Tongariro in New Zealand.

5.7. *Self-potential anomalies associated with the ascent of acidic groundwaters*

The case of active volcanoes characterized by very acid fumarolic fluids (especially strato-volcanoes, see Fig. 22) deserves a special attention. Two examples are provided in this section to illustrate the possible relationships between self-potential anomalies and

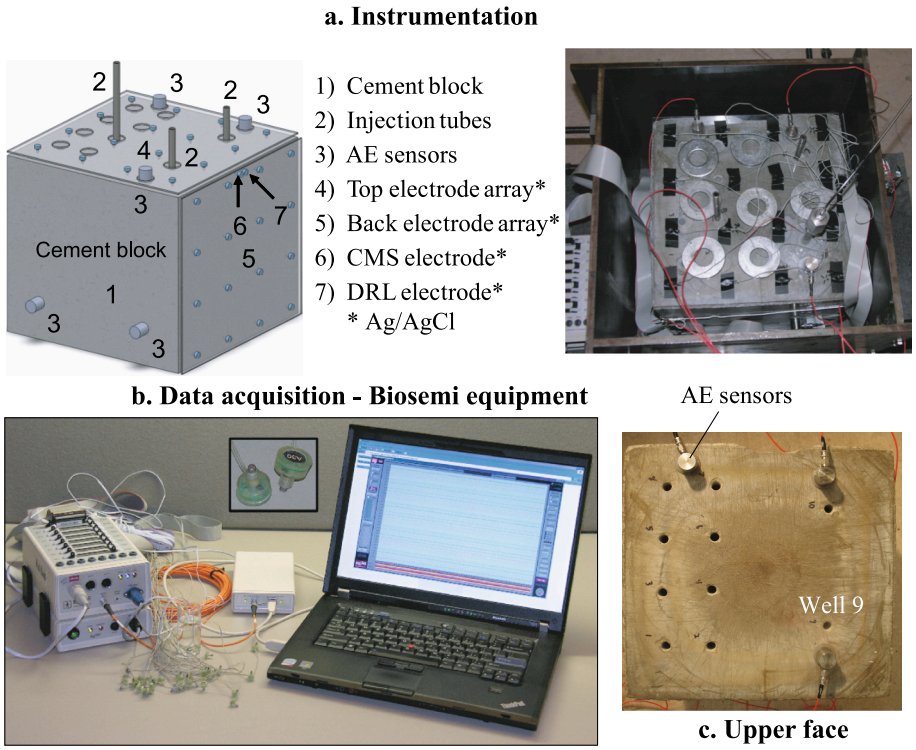

Fig. 25. Experimental setup used to follow hydromechanical disturbances using an array of self-potential electrodes and acoustic emission (AE) sensors. a. Porous cement block with the position of the wells, the AE sensors, and the electrode array. b. The self-potential signals are recorded with a very sensitive electroencephalographic voltmeter. The self-potential electrodes are 32 Ag/AgCl sintered electrodes. c. Position of the hydraulically stimulated well #9 and the three AE sensors on this face of the porous block. This experiment is similar to the monitoring of hydromechanical disturbances in a volcano at a larger scale. Modified from Haas et al. (2013).

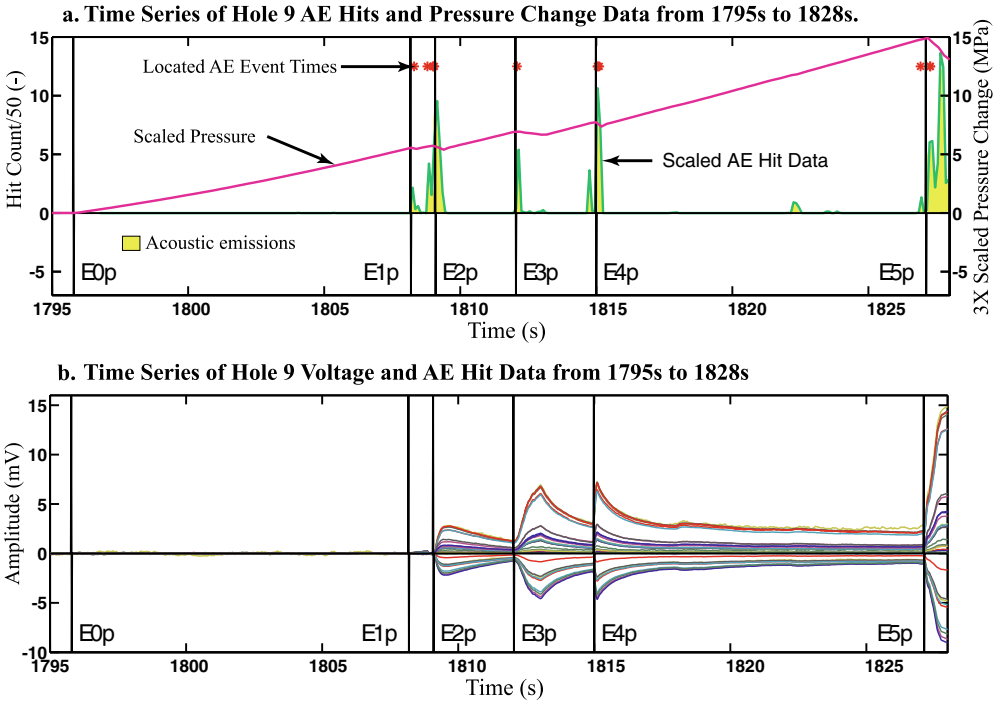

Fig. 26. Evolution of the fluid pressure, electrical potential changes, and acoustic emissions over time. a. The Acoustic Emissions (AEs) and fluid pressure disturbances occur at the same time. b. Self-potential time series recorded at the 32 electrodes of the array. All the signals indicate the existence of 6 hydromechanical disturbances labeled E0 to E5 with the build-up of fluid pressure, the formation of fractures, and the decay of the fluid pressure associated with the flow of the pore water in the cracks. Modified from Haas et al. (2013).

hydrothermal fluids with very low pH values: (i) the case of La Soufrière Volcano (Guadeloupe Island, France) and (ii) the case of Papandayan volcanoes (Java Island, Indonesia).

La Soufrière of Guadeloupe is characterized by the presence of a dome with fumarole activity where boiling ponds exhibit extremely acidic fluids (minimal pH ≈ -0.8) (Allard et al., 2014). Recent measurements also attest values of pH below pH = 1.0 in the summit area (Inostroza et al., 2022). A multi-method profile, 2430 m long, including self-potential measurements, soil temperature (at a depth of 30 cm), soil CO_2 concentration (at a depth of 30 cm), and electrical resistivity tomography were performed in the southern flank of La Soufrière dome. The profile was located between "North of Piton Tarade" on the Western side of the profile and the "Eastern flank of l'Echelle cone" on the Eastern side of the profile (labeled NPT and EFE, respectively in Fig. 23a).

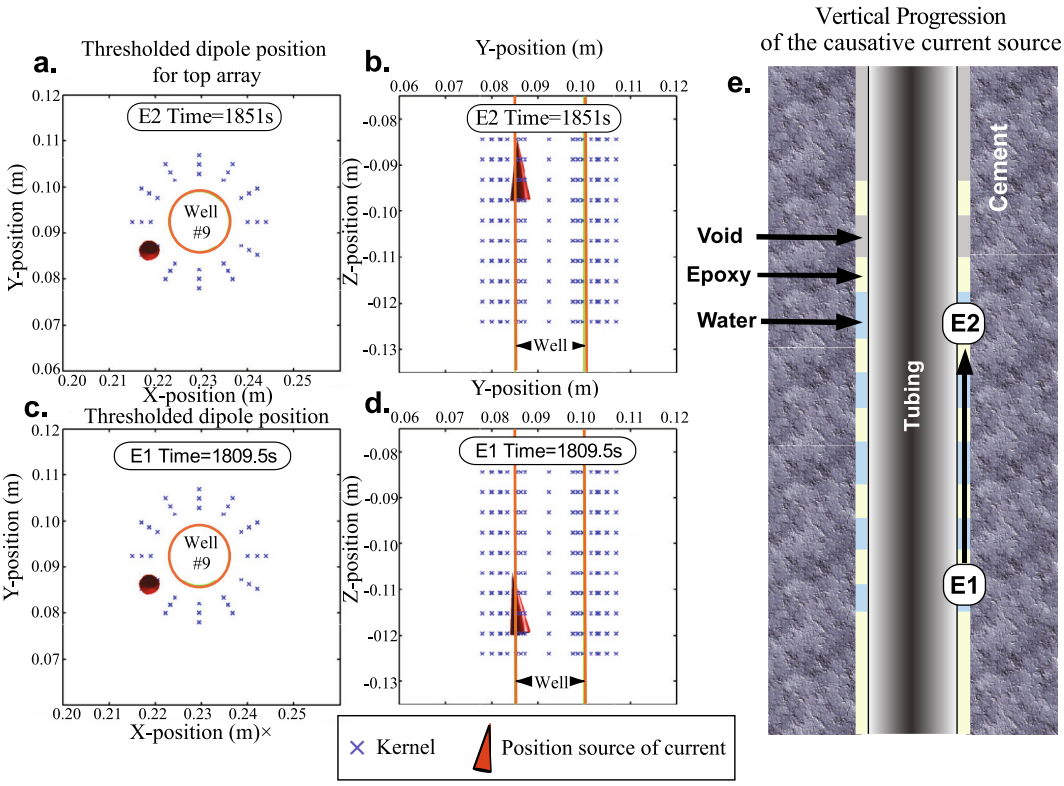

Fig. 27. Localization of a hydromechanical disturbance using transient self-potential signals. The inversion of the self-potential signals allow to demonstrate that the sources E1 and E2 are located in the vicinity of Hole #9 in panels a. to d. (arrows). e. Development of the hydromechanical disturbance along the hole breaking the epoxy connecting the well to the cement. These hydromechanical disturbances are responsible for the fluid pressure fluctuations, electrical impulses, and the acoustic emissions observed in Fig. 23. The inversion of the self-potential signals allows to invert not only the position of the events but also their magnitudes ($M_1 = 0.2$ mA m for Event E1 and $M_2 = 1.6$ mA for Event E2). The same type of signals could be observed on an active volcano and associated with thermo-hydromechanical disturbances in the vicinity of a magmatic conduit. Modified from Haas et al. (2013).

On the western side of the profile, the self-potential data display three self-potential minima consistent with the presence of three gullies (Type V, see pink stars PT-, DS2-, DS3- in Fig. 23b). Along this profile, one area, <200 m long, was affected by high temperature and CO_2 concentration anomalies (close to 100 °C and 100% respectively). These anomalies are associated with a shallow conductive area located along the La Ty fault, a system of regional active tectonic faults crossing the volcanic dome (see light grey colour rectangle on Fig. 23b). While we would expect a positive anomaly here, we observe no self-potential anomaly that could be associated with this upwelling of the hydrothermal fluids along the fault. The very low pH of the hydrothermal fluids is probably the cause of the absence of self-potential signature (see Fig. 5c showing that for acidic fluids, the streaming potential coupling coefficient is close to zero).

Another example showing a clear impact of the pH of the upwelling hydrothermal fluids on the self-potential signals was observed at Papandayan volcano (see Byrdina et al., 2018). The upwelling of the acidic fluids is marked by the electrically conductive bodies observed on the 3D-resistivity tomogram. The self-potential measurements shows a good correlation between the rising of hydrothermal fluids (see anomalies labeled A, B, and C in Fig. 24a) and the negative self-potential anomalies measured at the ground surface. The comparison between self-potential and soil pH provide an obvious positive correlation between these two parameters (see Fig. 24b). We can conclude that additional information such as the measurement of fluid or soil pH is critically needed to correctly interpret self-potential anomalies on strato-volcanoes.

5.8. *Transient self-potential anomaly*

In volcanic environments, self-potential anomalies can fluctuate over time in a broad spectrum of frequencies from few milliseconds to several months or years depending on the causative source of the signals. For instance, Kuwano et al. (2015) localized self-potential transient anomalies associated with very long period seicmic pulses (see also Byrdina et al., 2003).

Pride (1994) and Revil et al. (2015) show that the transient self-potential fluctuations are associated with any type of hydromechanical disturbances in partially water-saturated porous media. Revil et al. (2015) performed forward-modeling of these effects through the streaming current effect. They propose a laboratory experiment showing how these electrical fields can be recorded at the surface of a cement block during the hydromechanical stimulation of a well (Fig. 25). This experiment can be considered as an analog of the upflow of thermal water along a magmatic conduit or during the hydraulic stimulation of a well in a geothermal field. The laboratory measurements were performed with a very sensitive voltmeter corresponding to a medical electroencephalograph (Fig. 25). The signals were inverted using a genetic algorithm to localize the causative source of electrical current and therefore, localize the hydromechanical disturbance in the block (Figs. 26 and 27). Two snapshots of electrical signals were used to show how the position of the hydromechanical events evolved over time. The amplitude of the electric signals changed from the background level indicating that a volume of water was flowing in the close vicinity of the well producing fracking events at regular intervals (Fig. 27). Such approach can be used to monitor hydromechanical events in a geothermal system. This implies the development of repeated surveys or the development of continuous monitoring networks on volcanoes (e.g.,

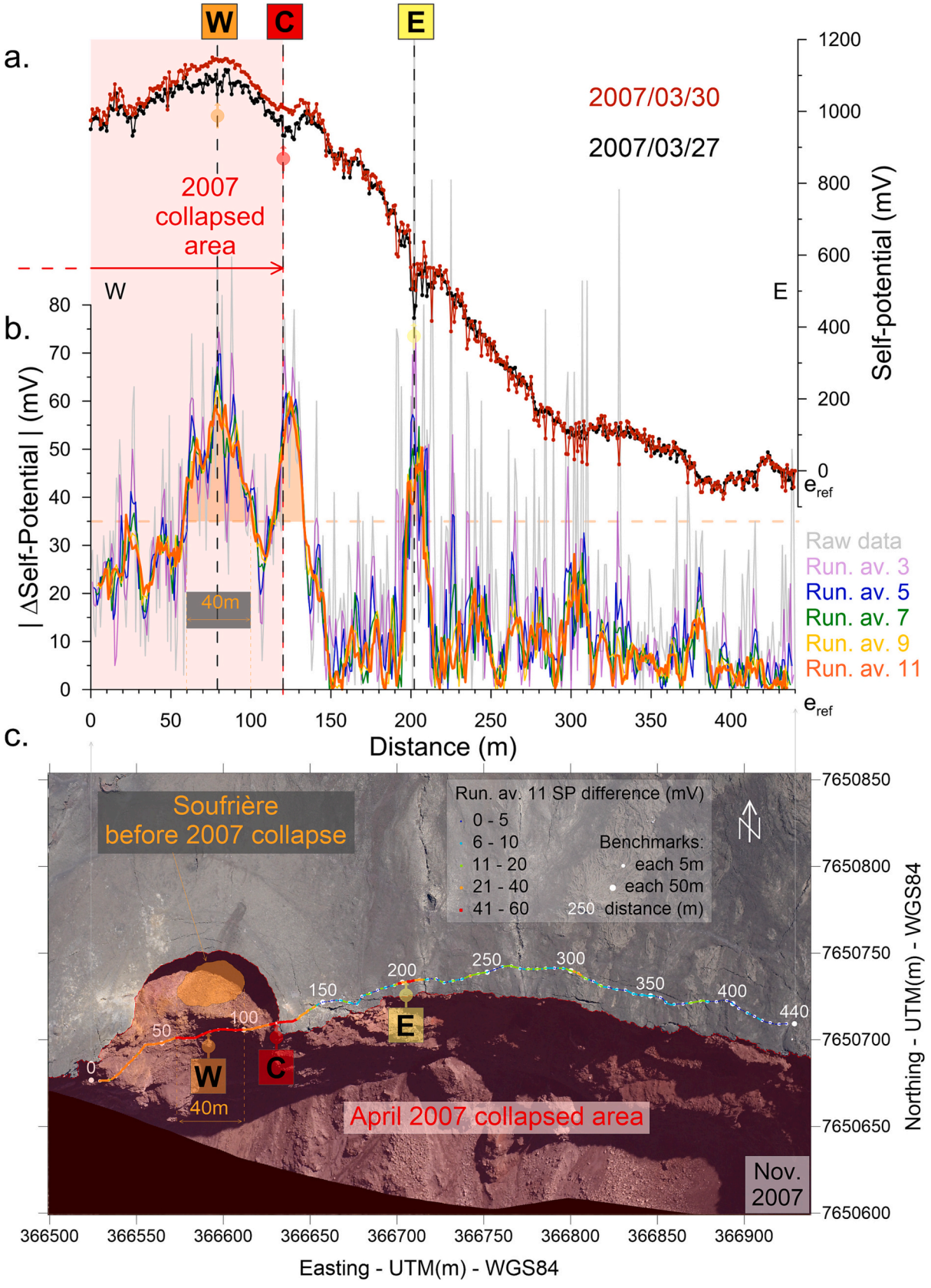

Fig. 28. Piton de la Fournaise volcano. a. Self-potential signal recorded along the profile, on March 27th and 30th 2007. b. Difference of self-potential between the two reiterations. Representation of the raw and filtered data using running averages over 3, 5, 7, 9, and 11 points. c. Aerial photograph of the studied area taken in November 2007 showing the collapsed area, the pre-collapse Soufrière pit crater, and the spatial distribution of SP anomalies along the profile. W, C, and E stand for western, central and eastern anomalies respectively (modified from Chaput et al., 2019).

Yasukawa et al., 2005; Matsushima et al., 2017).

Repeated self-potential surveys performed at Piton de la Fournaise volcano (Réunion Island, France) demonstrate how powerful the self-potential method is to detect with areas of mechanical weakness before the occurrence of a major destructive event in the caldera of this shield volcano. Based on a self-potential map performed over the entire cone of the Piton de la Fournaise volcano (Barde-Cabusson et al., 2012), a major self-potential positive anomaly located on the northern flank of the volcanic cone was chosen to install a reiteration profile, 440 m-long, with measurement point each meter along the profile (see details in Chaput et al., 2019, and Fig. 28c). The profile was reiterated twice, on 27 and 30 march 2007, few days before a major collapse in the caldera that occurred in April 5th to 7th, 2007 (see black and red data in Fig. 28a). The difference between these two self-potential reiterations displays three peaks corresponding to the maximum of difference (labeled "W", "C" and "E" in Fig. 28b). Different running average on the self-potential difference data allows to better visualize the self-potential changes. Two areas "W" and "C" correspond to a major difference in amplitude. The largest anomaly ("W", 40 m of lateral extension) corresponds to the size of the so-called Soufrière pit crater before the 2007 collapse. The anomaly "C" corresponds precisely to the boundary of the caldera that collapsed in April 2007. Therefore, the fluctuation in the self-potential signals can be used to evidence areas of high permeability and mechanical weakness, of a volcanic edifice. The mapping of these areas is very important in volcanology, to assess, on a spatial point of view, structural weaknesses of a volcanic edifice, which can evolve during volcanic crisis in caldera, flank or sector collapse.

This reiteration survey, performed each meter, demonstrates that interesting fluctuations in the self-potential signals can be measured only if one of the two electrodes is located over strategic areas ("W", "C" and "E" in our case). Two iterations of the profile is required. This result explains why permanent self-potential monitoring stations may remain blind to significant hydrothermal fluid disruptions is the electrodes are not correctly placed. Regarding permanent self-potential monitoring, it is interesting to mention Izu Oshima volcano (Japan), which has been continuously monitored from 2006 to 2014 (see Matsushima et al., 2017). A decrease in the self-potential signal (~100 mV) has been observed at Izu-Oshima in the years following the last eruption in 1986–1987 (Matsushima et al., 2017). This decrease was explained by the reduction in gas emissions. Subsequent self-potential variations are mostly periodic, resulting mainly from changes in the water table level due to precipitation. To better understand future self-potential precursor events, it will be necessary to measure the self-potential signal over one or several eruptive cycles.

6. Grand challenge

In our opinion, the next step to use self-potential signals to monitor active volcanoes is the integration of self-potential with electrical conductivity and induced polarization tomography. Great advances have been achieved recently in induced polarization tomography applied to active volcanoes (see a review in Revil and Gresse, 2021). First steps in the integration of self-potential and electrical conductivity tomography have been done recently for the localization of ore bodies below the sea floor at mid-oceanic ridges (Su et al., 2022). Combining physics based thermo-hydromechanical codes to simulate volcanic activity with time-lapse geoelectrical and electromagnetic (active and passive) methods together with passively collected seismic data would represent a breakthrough in our ability to monitor active volcanoes and predict their behavior in a way similar to weather forecasting. Some preliminary steps in this direction have been accomplished recently by Arens et al. (2022).

7. Conclusion

The flow of the groundwater in geothermal reservoirs and hydrothermal fields produces self-potential anomalies of several hundreds of millivolts and in some cases of several volts. The underlying physics of these anomalies is well-understood and the self-potential signals associated with groundwater flow can be easily forward-modeled. Furthermore, recent advances in the inverse problem can be used to assess the pattern of groundwater flow from self-potential signals in the realm of potential-field theory or coupled flow theory. In addition, we can model and invert the transient self-potential signals associated with fracking and hydro-mechanical disturbances, an important step in monitoring active volcanoes. The inversion of the self-potential signals can bring exciting information regarding the localization and the moment tensor of hydro-mechanical seismic events. It is therefore likely that the self-potential method could play an increasing role in the characterization of hydrothermal systems in volcanic areas in concert with borehole measurements, remote sensing, and other geophysical techniques. The joint inversion and interpretation of self-potential and induced polarization data appears promising.

Author contributions

The authors contributed equally to the research presented in this paper. All authors have read and agreed to the submitted version of the manuscript.

Funding

This research received no external funding.

Declaration of Competing Interest

The authors declare no conflict of interest. The funders had no role in the design of the study, in the collection, analyses, or interpretation of data, in the writing of the manuscript, or in the decision to publish the results.

Data availability

Data will be made available on request.

Acknowledgements

A. Revil thanks the CNRS for its support over the years. We thank the two referees and the Editor for their useful comments.

References

Ahmad, M.U., 1969. A laboratory study of streaming potentials. Geophys. Prospect. 12 (1), 49–64. https://doi.org/10.1111/j.1365-2478.1964.tb01889.x.

Aizawa, K., 2000. Classification of self-potential anomalies on volcanoes and possible interpretations for their subsurface structure. J. Volcanol. Geotherm. Res. 175, 253–268. https://doi.org/10.1016/j.jvolgeores.2008.03.011.

Aizawa, K., 2004. A large self-potential anomaly and its changes on the quiet Mt. Fuji, Japan. Geophys. Res. Lett. 31 (5) https://doi.org/10.1029/2004GL019462.

Aizawa, K., Yoshimura, R., Oshiman, N., Yamazaki, K., Uto, T., Ogawa, Y., Hurst, W.A., 2005. Hydrothermal system beneath Mt. Fuji volcano inferred from magnetotellurics and electric self-potential. Earth Planet. Sci. Lett. 235 (1–2), 343–355. https://doi.org/10.1016/j.epsl.2005.03.023.

Aizawa, K., Ogawa, Y., Ishido, T., 2009. Groundwater flow and hydrothermal systems within volcanic edifices: delineation by electric self-potential and magnetotellurics. J. Geophys. Res. Solid Earth 114 (B1), B01208. https://doi.org/10.1029/2008JB005910.

Alarouj, M., Collini, H., Jackson, M.D., 2021a. Positive zeta potential in sandstones saturated with natural saline brine. Geophys. Res. Lett. 48 https://doi.org/10.1029/2021GL094306 e2021GL094306.

Alarouj, M., Ijioma, A., Graham, M.T., MacAllister, D.J., Jackson, M.D., 2021b. Numerical modelling of self-potential in subsurface reservoirs. Comput. Geosci. 146, 104656 https://doi.org/10.1016/j.cageo.2020.104656.

Allard, P., Aiuppa, A., Beauducel, F., Gaudin, D., Di Napoli, R., Calabrese, S., Tamburello, G., 2014. Steam and gas emission rate from La Soufriere volcano, Guadeloupe (Lesser Antilles): implications for the magmatic supply during degassing unrest. Chem. Geol. 384, 76–93. https://doi.org/10.1016/j.chemgeo.2014.06.019.

Anderson, L.A., Johnson, C.R., 1976. Application of the self-potential method to geothermal exploration in Long Valley, California. J. Geophys. Res. 81, 1527–1532. https://doi.org/10.1029/JB081I008P01527.

Arens, F., Gottsmann, J., Strehlow, K., Hickey, J., Kilgour, G., 2020. Electrokinetic contributions to self-potential signals from magmatic stressing. Geochem. Geophys. Geosyst. 21 (12), 1–21. https://doi.org/10.1029/2020GC009388.

Arens, F., Coco, A., Gottsmann, J., Hickey, J., Kilgour, G., 2022. Multiphysics modeling of volcanic unrest at Mt. Ruapehu (New Zealand). Geochem. Geophys. Geosyst. 23 https://doi.org/10.1029/2022GC010572 e2022GC010572.

Aubert, M., Dana, I., 1994. Interpretation of the self-potential radial profiles in volcanology: Possibilities of the SP method for the monitoring of the active volcanoes. Bulletin de la Société Géologique de France 2, 113–122.

Aubert, M., Dana, I.N., Livet, M., 1990. Vérification des limites de nappes aquifères en terrain volcanique par la méthode de polarisation spontanée. C.R.Ac.Sc. Paris 311, 999–1004.

Avena, M.J., De Pauli, C.P., 1998. Proton adsorption and electrokinetics of an Argentinean Montmorillonite. J. Colloid Interface Sci. 202, 195–204. https://doi.org/10.1006/jcis.1998.5402.

Barde, Cabusson S., Finizola, A., Grobbe, N., 2021. A practical approach for self-potential data acquisition, processing and visualization. Interpretation. 9 (1) https://doi.org/10.1190/INT-2020-0012.1.

Barde-Cabusson, S., Levieux, G., Lénat, J.F., Finizola, A., Revil, A., Chaput, M., Vieille, M., 2009a. Transient self-potential anomalies associated with recent lava flows at Piton de la Fournaise volcano (Réunion Island, Indian Ocean). J. Volcanol. Geotherm. Res. 187 (3–4), 158–166. https://doi.org/10.1016/j.jvolgeores.2009.09.003.

Barde-Cabusson, S., Finizola, A., Revil, A., Ricci, T., Piscitelli, S., Rizzo, E., Villeneuve, N., 2009b. New geological insights and structural control on fluid circulation in La Fossa cone (Vulcano, Aeolian Islands, Italy). J. Volcanol. Geotherm. Res. 185 (3), 231–245. https://doi.org/10.1016/j.jvolgeores.2009.06.002.

Barde-Cabusson, S., Finizola, A., Peltier, A., Chaput, M., Taquet, N., Dumont, S., Duputel, Z., Guy, A., Mathieu, L., Saumet, S., Sorbadère, F., Vieille, M., 2012. Structural control of collapse events inferred by self-potential mapping on the Piton de la Fournaise volcano (La Réunion Island). J. Volcanol. Geotherm. Res. 209-210, 9–18. https://doi.org/10.1016/j.jvolgeores.2011.09.014.

Bennati, L., Finizola, A., Walker, J., Lopez, D., Higuiera-Diaz, C., Schütze, C., Barahona, F., Cartagena, R., Conde, V., Funes, R., Rios, C., 2011. Fluid circulation in a complex volcano-tectonic setting, inferred from self-potential and soil CO_2 flux surveys: the Santa María - Cerro Quemado – Zunil volcanoes and Xela caldera (northwestern Guatemala). J. Volcanol. Geotherm. Res. 199, 216–229. https://doi.org/10.1016/j.jvolgeores.2010.11.008.

Bogoslovsky, V.A., Ogilvy, A.A., 1973. Deformations of natural electric fields near drainage structures. Geophys. Prospect. 21, 716–723. https://doi.org/10.1111/j.1365-2478.1973.tb00053.x.

Bolève, A., Revil, A., Janod, F., Mattiuzzo, J.L., Jardani, A., 2007a. Forward modeling and validation of a new formulation to compute self-potential signals associated with ground water flow. Hydrol. Earth Syst. Sci. 11 (5), 1661–1671. https://doi.org/10.5194/hess-11-1661-2007.

Bolève, A., Crespy, A., Revil, A., Janod, F., Mattiuzzo, J.L., 2007b. Streaming potentials of granular media: influence of the Dukhin and Reynolds numbers. J. Geophys. Res. Solid Earth 112 (B8). https://doi.org/10.1029/2006JB004673.

Bolève, A., Janod, F., Revil, A., Lafon, A., Fry, J.-J., 2011. Localization and quantification of leakages in dams using time-lapse self-potential measurements associated with salt tracer injection. J. Hydrol. 403 (3–4), 242–252. https://doi.org/10.1016/j.jhydrol.2011.04.008.

Brothelande, E., Finizola, A., Peltier, A., Delcher, E., Komorowski, J.C., Di Gangi, F., Legendre, Y., 2014. Fluid circulation pattern inside La Soufrière volcano (Guadeloupe) inferred from combined electrical resistivity tomography, self-potential, soil temperature and diffuse degassing measurements. J. Volcanol. Geotherm. Res. 288, 105–122. https://doi.org/10.1016/j.jvolgeores.2014.10.007.

Bull, H.B., Gortner, R.A., 1932. Electrokinetic potentials. X. The effect of particle size on potentials. J. Phys. Chem. 36, 111–119. https://doi.org/10.1021/j150331a007.

Byrdina, S., Friedel, S., Wassermann, J., Zlotnicki, J., 2003. Self-potential variations associated with ultra-long-period seismic signals at Merapi volcano. Geophys. Res. Lett. 30 (22), 2156. https://doi.org/10.1029/2003GL018272.

Byrdina, S., Ramos, D., Vandemeulebrouck, J., Masias, P., Revil, A., Finizola, A., Macedo, O., 2013. Influence of the regional topography on the remote emplacement of hydrothermal systems with examples of Ticsani and Ubinas volcanoes, Southern Peru. Earth Planet. Sci. Lett. 365, 152–164. https://doi.org/10.1016/j.epsl.2013.01.018.

Byrdina, S., Grandis, H., Sumintadireja, P., Caudron, C., Syahbana, D.K., Naffrechoux, E., Vandemeulebrouck, J., 2018. Structure of the acid hydrothermal system of Papandayan volcano, Indonesia, investigated by geophysical methods. J. Volcanol. Geotherm. Res. 358, 77–86. https://doi.org/10.1016/j.jvolgeores.2018.06.008.

Casagrande, L., 1983. Stabilization of soils by means of electro-osmosis: state of the art. J. Boston Soc. Civ. Eng. 69 (2), 255–302.

Chaput, M., Finizola, A., Peltier, A., Villeneuve, N., Crovisier, M., Barde-Cabusson, S., 2019. Where does a volcano break? Using self-potential reiteration to forecast the precise location of major destructive events on active volcanoes: the case study of the Piton de la Fournaise 2007 caldera collapse. Volcanica 2 (2), 151–159. https://doi.org/10.30909/vol.02.02.151159.

Corwin, R.F., Hoover, D.B., 1979. The self-potential method in geothermal exploration. Geophysics 44, 226–245. https://doi.org/10.1190/1.1440964.

Corwin, A.F., Morrison, H.F., Diaz, C.S., Rodriguez, B.J., 1979. Self.potential studies at the Cerro Prieto geothermal field. In: Proceedings, First Symposium on the Cerro Prieto geothermal field, Baja California, Mexico, September 1978, 7098. Lawrence Berkeley Laboratory. LBL, Berkeley, pp. 204–210.

Di Maio, R., Mauriello, P., Patella, D., Petrillo, Z., Piscitelli, S., Siniscalchi, A., 1998. Electric and electromagnetic outline of the Mount Somma–Vesuvius structural setting. J. Volcanol. Geotherm. Res. 82, 219–238. https://doi.org/10.1016/S0377-0273(97)00066-8.

Dorfman, N.H., Oskay, M.M., Gaddis, M.P., 1977. Self-potential profiling: a new technique for determination of heat movement in a thermal oil recovery flood. In: Preprint presented at 52nd Ann. Meeting, SPE of AIME, Denver.

Erickson, D., Li, D., 2001. Streaming potential and streaming current methods for characterizing heterogeneous solid surfaces. J. Colloid Interface Sci. 237, 283–289. https://doi.org/10.1006/jcis.2001.7476.

Finizola, A., Sortino, F., Lénat, J.-F., Valenza, M., 2002. Fluid circulation at Stromboli volcano (Aeolian Islands, Italy) from self-potential and soil gas surveys. J. Volcanol. Geotherm. Res. 116 (1–2), 1–18. https://doi.org/10.1016/S0377-0273(01)00327-4.

Finizola, A., Sortino, F., Lénat, J.-F., Aubert, M., Ripepe, M., Valenza, M., 2003. The summit hydrothermal system of Stromboli: new insights from self-potential, temperature, CO_2 and fumarolic fluids measurements, with structural and monitoring implications. Bull. Volcanol. 65, 486–504. https://doi.org/10.1007/s00445-003-0276-z.

Finizola, A., Lénat, J.-F., Macedo, O., Ramos, D., Thouret, J.-C., Sortino, F., 2004. Fluid circulation and structural discontinuities inside Misti volcano (Peru) inferred from self-potential measurements. J. Volcanol. Geotherm. Res. 135 (4), 343–360. https://doi.org/10.1016/j.jvolgeores.2004.03.009.

Finizola, A., Aubert, M., Revil, A., Schütze, C., Sortino, F., 2009. Importance of structural history in the summit area of Stromboli during the 2002–2003 eruptive crisis inferred from temperature, soil CO_2, self-potential, and electrical resistivity tomography. J. Volcanol. Geotherm. Res. 183, 213–227. https://doi.org/10.1016/j.jvolgeores.2009.04.002.

Fournier, C., 1989. Spontaneous potentials and resistivity surveys applied to hydrogeology in a volcanic area: case history of the Chaîne des Puys (Puy-de-Dôme, France). Geophys. Prospect. 37, 647–668. https://doi.org/10.1111/j.1365-2478.1989.tb02228.x.

Fox, R.W., 1830. On the electromagnetic properties of metalliferous veins in the mines of Cornwall. Philos. Trans. R. Soc. 120, 399–414.

Friborg, J., 1996. Experimental and Theoretical Investigations into the Streaming Potential Phenomenon with Special Reference to Applications in Glaciated Terrain. Ph.D. thesis. Lulea University of Technology, Sweden.

Furness, P., 1994. A finite difference model for mineral self-potentials in complex environments. J. Appl. Geophys. 32, 235–243. https://doi.org/10.1016/0926-9851(94)90024-8.

Gascuel, V., Bédard, K., Comeau, F.A., Raymond, J., Malo, M., 2020. Geothermal resource assessment of remote sedimentary basins with sparse data: lessons learned from Anticosti Island. Canada. Geotherm. Energy 8 (3). https://doi.org/10.1186/s40517-020-0156-1.

Gex, P., 1980. Electrofiltration phenomena associated with several dam sites. Bull. Soc. Vaud Sci. Nat. 357 (75), 39–50.

Gonzales, K., Finizola, A., Lénat, J.-F., Macedo, O., Ramos, D., Thouret, J.-C., Fournier, N., Cruz, V., Pistre, K., 2014. Asymmetrical structure, hydrothermal system and edifice stability: the case of Ubinas volcano, Peru, revealed by geophysical surveys. J. Volcanol. Geotherm. Res. 276, 132–144. https://doi.org/10.1016/j.jvolgeores.2014.02.020.

Goodfellow, W.D., 2007. Metallogeny of the Bathurst mining camp, northern New Brunswick. In: Goodfellow, W.D. (Ed.), Mineral Deposits of Canada—A Synthesis of Major Deposit-Types, District Metallogeny, the Evolution of Geological Provinces, and Exploration Methods, 5. Geological Association of Canada, Mineral Deposits Division, Special Publication, pp. 449–469.

Grech, R., Cassar, T., Muscat, J., Camilleri, K.P., Fabri, S.G., Zervakis, M., Xanthopoulos, P., Sakkalis, V., Vanrumste, B., 2008. Review on solving the inverse problem in EEG source analysis. J. NeuroEng. Rehab. 5 (25), 1–33. https://doi.org/10.1186/1743-0003-5-25.

Gresse, M., Uyeshima, M., Koyama, T., Hase, H., Aizawa, K., Yamaya, Y., Hata, M., 2021. Hydrothermal and magmatic system of a volcanic island inferred from magnetotellurics, seismicity, self-potential, and thermal image: an example of Miyakejima (Japan). J. Geophys. Res. Solid Earth 126 (6). https://doi.org/10.1029/2021JB022034 e2021JB022034.

Guo, H., Keppler, H., 2019. Electrical conductivity of NaCl-bearing aqueous fluids to 900 C and 5 GPa. J. Geophys. Res. Solid Earth 124 (2), 1397–1411. https://doi.org/10.1029/2018JB016658.

Haas, A.K., Revil, A., Karaoulis, M., Frash, L., Hampton, J., Gutierrez, M., Mooney, M., 2013. Electrical potential source localization reveals a borehole leak during hydraulic fracturing. Geophysics 78 (2), D93–D113. https://doi.org/10.1190/GEO2012-0388.1.

Hase, H., Hashimoto, T., Sakanaka, S., Kanda, W., Tanaka, Y., 2005. Hydrothermal system beneath Aso volcano as inferred from self-potential mapping and resistivity structure. J. Volcanol. Geotherm. Res. 143, 259–277. https://doi.org/10.1016/j.jvolgeores.2004.12.005.

Helmholz, H., 1879. Study concerning electrical boundary layers. Weidemann Annalen der Physik u. Chem. 3rd Ser. 7, 337–382.

Huenges, E., 2010. Geothermal energy systems: exploration, development, and utilization, 487 pp. Wiley. https://doi.org/10.1002/9783527630479.

Inostroza, M., Moune, S., Moretti, R., Robert, V., Bonifacie, M., Chilin-Eusebe, E., Burckel, P., 2022. Monitoring hydrothermal activity using major and trace elements in low-temperature fumarolic condensates: the case of La Soufriere de Guadeloupe Volcano. Geosciences 12 (7), 267. https://doi.org/10.3390/geosciences12070267.

Ishido, T., 2004. Electrokinetic mechanism for the "W"-shaped self-potential profile on volcanoes. Geophys. Res. Lett. 31 (15) https://doi.org/10.1029/2004GL020409.
Ishido, T., Mizutani, H., 1981. Experimental and theoretical basis of electrokinetic phenomena in rock-water systems and its application to geophysics. J. Geophys. Res. 86, 1763–1775. https://doi.org/10.1029/JB086iB03p01763.
Ishido, T., Pritchett, J.W., 1999. Numerical simulation of electrokinetic potentials associated with subsurface fluid flow. J. Geophys. Res. Solid Earth 104 (B7), 15247–15259. https://doi.org/10.1029/1999JB900093.
Ishido, T., Kikuchi, T., Matsushima, N., Yano, Y., Nakao, S., Sugihara, M., Tosha, T., Takakura, S., Ogawa, Y., 1997. Repeated self-potential profiling of Izu-Oshima volcano, Japan. J. Geomagn. Geoelectr. 49 (11−12), 1267–1278. https://doi.org/10.5636/jgg.49.1267.
Jackson, M.D., 2008. Characterization of multiphase electrokinetic coupling using a bundle of capillary tubes model. J. Geophys. Res. 113, B04201. https://doi.org/10.1029/2007JB005490.
Jackson, M.D., 2010. Multiphase electrokinetic coupling: insights into the impact of fluid and charge distribution at the pore scale from a bundle of capillary tubes model. J. Geophys. Res. 115, B07206. https://doi.org/10.1029/2009JB007092.
Jardani, A., Revil, A., 2009a. Stochastic joint inversion of temperature and self-potential data. Geophys. J. Int. 179 (1), 640–654. https://doi.org/10.1111/j.1365-246X.2009.04295.x.
Jardani, A., Revil, A., 2009b. Stochastic joint inversion of temperature and self-potential data. Geophys. J. Int. 179 (1), 640–654. https://doi.org/10.1111/j.1365-246X.2009.04295.x.
Jardani, A., Revil, A., Bolève, A., Dupont, J.P., Barrash, W., Malama, B., 2007. Tomography of the Darcy velocity from self-potential measurements. Geophys. Res. Lett. 34, L24403. https://doi.org/10.1029/2007GL031907.
Jardani, A., Revil, A., Bolève, A., Dupont, J.P., 2008. 3D inversion of self-potential data used to constrain the pattern of ground water flow in geothermal fields. J. Geophys. Res. 113, B09204. https://doi.org/10.1029/2007JB005302.
Jolie, E., Scott, S., Faulds, J., Chambefort, I., Axelsson, G., Gutiérrez-Negrín, L.C., Zemedkun, M.T., 2021. Geological controls on geothermal resources for power generation. Nart. Rev. Earth Environ. 2 (5), 324–339. https://doi.org/10.1038/s43017-021-00154-y.
Jougnot, D., Linde, N., Revil, A., Doussan, C., 2012. Derivation of soil-specific streaming potential electrical parameters from hydrodynamic characteristics of partially saturated soils. Vadoze Zone J. 11 (1) https://doi.org/10.2136/vzj2011.0086.
Jougnot, D., Thanh, L.D., Soldi, M., Vinogradov, J., Guarracino, L., 2021. Advances and benefits of fractal models to predict streaming potentials in partially saturated porous media. In: EGU General Assembly 2021, EGU21–10835. https://doi.org/10.5194/egusphere-egu21-10835.
Jouniaux, L., Maineult, A., Naudet, V., Pessel, M., Sailhac, P., 2009. Review of self-potential methods in hydrogeophysics. C. R. Geosci. 341, 928–936.
Keller, G.V., 1981. Exploration for geothermal energy. In: Fitch, A.A. (Ed.), Developments in Geophysical Exploration. Methods – 2. Applied Science Pub, pp. 107–150.
Kushnir, A., Loewer, M., 2020. From exploration to operation: research developments in deep geothermal energy. Geotherm. Energy 8 (15). https://doi.org/10.1186/s40517-020-00169-6.
Kuwano, O., Yoshida, S., Nakatani, M., Uyeshima, M., 2015. Origin of transient self-potential signals associated with very long period seismic pulses observed during the 2000 activity of Miyakejima volcano. J. Geophys. Res. Solid Earth 120 (5), 3544–3565. https://doi.org/10.1002/2014JB011740.
Leinov, E., Vinogradov, J., Jackson, M.D., 2010. Salinity dependence of the thermoelectric coupling coefficient in brine-saturated sandstones. Geophys. Res. Lett. 37 (23), L23308. https://doi.org/10.1029/2010GL045379.
Long, H.L., Hao, J.Q., 2005. Theoretical and experimental research on self-potential tomography. Chin. J. Geophys. Chin. Ed. 48 (6), 1343–1349. https://doi.org/10.1002/cjg2.789.
Lu, S.-M., 2018. A global review of enhanced geothermal system (EGS). Renew. Sust. Energ. Rev. 81, 2902–2921. https://doi.org/10.1016/j.rser.2017.06.097.
Mahardika, H., Revil, A., Jardani, A., 2012. Waveform joint inversion of seismograms and electrograms for moment tensor characterization of fracking events. Geophysics 77 (5), ID23-ID39. https://doi.org/10.1190/GEO2012-0019.1.
Maineult, A., Bernabé, Y., Ackerer, P., 2005. Detection of advected concentration and pH fronts from self-potential measurements. J. Geophys. Res. 110 (B11), B11205. https://doi.org/10.1029/2005JB003824.
Maineult, A., Bernabé, Y., Ackerer, P., 2006. Detection of advected, reacting redox fronts from self-potential measurements. J. Contam. Hydrol. 86 (1–2), 32–52. https://doi.org/10.1016/j.jconhyd.2006.02.007.
Malama, B., Revil, A., Kulhman, K.L., 2009a. A semi-analytical solution for transient streaming potentials associated with confined aquifer pumping tests. Geophys. J. Int. 176, 1007–1016. https://doi.org/10.1111/j.1365-246X.2008.04014.x.
Malama, B., Kuhlman, K.L., Revil, A., 2009b. Theory of transient streaming potentials associated with axial-symmetric flow in unconfined aquifers. Geophys. J. Int. 179, 990–1003. https://doi.org/10.1111/j.1365-246X.2009.04336.x.
Matsushima, N., Nishi, Y., Onizawa, S.Y., Takakura, S., Hase, H., Ishido, T., 2017. Self-potential characteristics of the dormant period of Izu-Oshima volcano. Bull. Volcanol. 79 (12), 86. https://doi.org/10.1007/s00445-017-1173-1.
Mazot, A., Bernard, A., Fischer, T., Inguaggiato, S., Sutawidjaja, I.S., 2008. Chemical evolution of thermal waters and changes in the hydrothermal system of Papandayan volcano (West Java, Indonesia) after the November 2002 eruption. J. Volcanol. Geotherm. Res. 178 (2), 276–286. https://doi.org/10.1016/j.jvolgeores.2008.06.022.
Mendonça, C.A., 2008. Forward and inverse self-potential modeling in mineral exploration. Geophysics 73 (1), F33–F43. https://doi.org/10.1190/1.2821191.
Miller, C.A., Kang, S.G., Fournier, D., Hill, G., 2018. Distribution of and condensate in a hydrothermal system: insights from self-potential inversion at Mount Tongariro, New Zealand. Geophys. Res. Lett. 45, 8190–8198. https://doi.org/10.1029/2018GL078780.
Moore, J.R., Glaser, S.D., 2007. Self-potential observations during hydraulic fracturing. J. Geophys. Res. 112, B02204. https://doi.org/10.1029/2006JB004373.
Nourbehecht, B., 1963. Irreversible Thermodynamic Effects in Inhomogeneous Media and their Application in Certain Geoelectric Problems. Ph.D. Thesis. MIT, Cambridge.
Onizawa, S.Y., Matsushima, N., Ishido, T., Hase, H., Takakura, S., Nishi, Y., 2009. Self-potential distribution on active volcano controlled by three-dimensional resistivity structure in Izu-Oshima, Japan. Geophys. J. Int. 178 (2), 1164–1181. https://doi.org/10.1111/j.1365-246X.2009.04203.x.
Patella, D., 1997a. Introduction to ground surface self-potential tomography. Geophys. Prospect. 45, 653–681. https://doi.org/10.1046/j.1365-2478.1997.430277.x.
Patella, D., 1997b. Self-potential global tomography including topographic effects. Geophys. Prospect. 45, 843. https://doi.org/10.1046/j.1365-2478.1997.570296.x.
Pengra, D., Li, S.X., Wong, P., 1999. Determination of rock properties by low-frequency AC electrokinetics. J. Geophys. Res. 104, 485–508. https://doi.org/10.1029/1999JB900277.
Petiau, G., 2000. Second generation of lead-lead chloride electrodes for geophysical applications. Pure Appl. Geophys. 3, 357–382. https://doi.org/10.1007/s000240050004.
Petiau, G., Dupis, A., 1980. Noise, temperature coefficient and long time stability of electrodes for telluric observations. Geophys. Prospect. 28 (5), 792–804. https://doi.org/10.1111/j.1365-2478.1980.tb01261.x.
Pokrovsky, O.S., Schott, J., Thomas, F., 1999. Dolomite surface speciation and reactivity in aquatic systems. Geochim. Cosmochim. Acta 63, 3133–3143. https://doi.org/10.1016/S0016-7037(99)00240-9.
Poldini, E., 1938. Geophysical exploration by spontaneous polarization methods. Min. Mag. 59, 278–282, 347–352. https://archive-ouverte.unige.ch/unige:157459.
Poldini, E., 1939. Geophysical exploration by spontaneous polarization methods. Min. Mag. 60, 22–27, 90–94. https://archive-ouverte.unige.ch/unige:157459.
Pride, S., 1994. Governing equations for the coupled electromagnetics and acoustics of porous media. Phys. Rev. B 50, 15678–15696. https://doi.org/10.1103/PhysRevB.50.15678.
Quincke, G., 1859. Concerning a new type of electrical current. Ann. Phys. Chem. 107, 1–47.
Reinsch, T., Dobson, P., Asanuma, H., Huenges, E., Poletto, F., Sanjuan, B., 2017. Utilizing supercritical geothermal systems: a review of past ventures and ongoing research activities. Geotherm. Energy 5 (1), 16. https://doi.org/10.1186/s40517-017-0075-y.
Revil, A., 1999. Ionic diffusivity, electrical conductivity, membrane and thermoelectric potentials in colloids and granular porous media: a unified model. J. Colloid Interface Sci. 212, 503–522. https://doi.org/10.1006/jcis.1998.6077.
Revil, A., 2010. Comment on "Review of self-potential methods in hydrogeophysics" by L. Jouniaux, A. Maineult, V. Naudet, M. Pessel, and P. Sailhac. C.R. Geosci. 342 (10), 807–809.
Revil, A., Florsch, N., 2010. Determination of permeability from spectral induced polarization in granular media. Geophys. J. Int. 181 (3), 1480–1498. https://doi.org/10.1111/j.1365-246X.2010.04573.x.
Revil, A., Gresse, M., 2021. Induced polarization as a tool to assess alteration in volcanic areas: a review. Minerals 11 (9), 962. https://doi.org/10.3390/min11090962.
Revil, A., Jardani, A., 2013. The Self-Potential Method: Theory and Applications in Environmental Geosciences. Cambridge University Press.
Revil, A., Linde, N., 2006. Chemico-electromechanical coupling in microporous media. J. Colloid Interface Sci. 302, 682–694. https://doi.org/10.1016/j.jcis.2006.06.051.
Revil, A., Pezard, P.A., 1998a. Streaming electrical potential anomaly along faults in geothermal areas. Geophys. Res. Lett. 25 (16), 3197–3200. https://doi.org/10.1029/98GL02384.
Revil, A., Pezard, P.A., 1998b. Streaming electrical potential anomaly along faults in geothermal areas. Geophys. Res. Lett. 25 (16), 3197–3200. https://doi.org/10.1029/98GL02384.
Revil, A., Pezard, P.A., Glover, P.W.J., 1999a. Streaming potential in porous media. 1. Theory of the zeta-potential. J. Geophys. Res. 104 (B9), 20,021–20,031. https://doi.org/10.1029/1999JB900089.
Revil, A., Schwaeger, H., Cathles, L.M., Manhardt, P., 1999b. Streaming potential in porous media. 2. Theory and application to geothermal systems. J. Geophys. Res. 104 (B9), 20,033–20,048. https://doi.org/10.1029/1999JB900090.
Revil, A., Naudet, V., Nouzaret, J., Pessel, M., 2003. Principles of electrography applied to self-potential electrokinetic sources and hydrogeological applications. Water Resour. Res. 39 (5), 1114. https://doi.org/10.1029/2001WR000916.
Revil, A., Finizola, A., Sortino, F., Ripepe, M., 2004. Geophysical investigations at Stromboli volcano, Italy. Implications for ground water flow and paroxysmal activity. Geophys. J. Int. 157, 426–440. https://doi.org/10.1111/j.1365-246X.2004.02181.x.
Revil, A., Fan, Q., Cary, L., Finizola, A., Trolard, F., 2005a. Self-potential signals associated with preferential ground water flow pathways in a buried paleo-channel. Geophys. Res. Lett. 32, L07401. https://doi.org/10.1029/2004GL022124.
Revil, A., Leroy, P., Titov, K., 2005b. Characterization of transport properties of argillaceous sediments. Application to the Callovo-Oxfordian argillite. J. Geophys. Res. 110, B06202. https://doi.org/10.1029/2004JB003442.
Revil, A., Linde, N., Cerepi, A., Jougnot, D., Matthäi, S., Finsterle, S., 2007. Electrokinetic coupling in unsaturated porous media. J. Colloid Interface Sci. 313 (1), 315–327. https://doi.org/10.1016/j.jcis.2007.03.037.

Revil, A., Finizola, A., Piscitelli, A., Rizzo, E., Ricci, T., Crespy, A., Angeletti, B., Balasco, M., Barde, Cabusson S., Bennati, L., Bolève, A., Byrdina, S., Carzaniga, N., Di Gangi, F., Morin, J., Perrone, A., Rossi, M., Roulleau, E., Suski, B., 2008. Inner structure of La Fossa di Vulcano (Vulcano Island, southern Tyrrhenian Sea, Italy) revealed by high resolution electric resistivity tomography coupled with self-potential, temperature, and soil CO_2 diffuse degassing measurements. J. Geophys. Res. 113, B07207. https://doi.org/10.1029/2007JB005394.

Revil, A., Johnson, T.C., Finizola, A., 2010a. Three-dimensional resistivity tomography of Vulcan's forge, Vulcano Island, southern Italy. Geophys. Res. Lett. 37 (15) https://doi.org/10.1029/2010GL043983.

Revil, A., Johnson, T.C., Finizola, A., 2010b. Three-dimensional resistivity tomography of Vulcan's forge, Vulcano Island, southern Italy. Geophys. Res. Lett. 37, L15308. https://doi.org/10.1029/2010GL043983.

Revil, A., Karaoulis, M., Srivastava, S., Byrdina, S., 2013a. Thermoelectric self-potential and resistivity data localize the burning front of underground coal fires. Geophysics 78 (5), B259–B273. https://doi.org/10.1190/geo2013-0013.1.

Revil, A., Skold, M., Hubbard, S., Wu, Y., Watson, D., Karaoulis, M., 2013b. Petrophysical properties of saprolites from the Oak Ridge Integrated Field Research Challenge site, Tennessee. Geophysics 78 (1), D21–D40. https://doi.org/10.1190/geo2012-0176.1.

Revil, A., Mao, D., Haas, A.K., Karaoulis, M., Frash, L., 2015. Passive electrical monitoring and localization of leakages in wells using electrography. J. Hydrol. 521, 286–301. https://doi.org/10.1016/j.jhydrol.2014.12.003.

Revil, A., Meyer, C.D., Niu, Q., 2016. A laboratory investigation of the thermoelectric effect. Geophysics 81 (4), E243–E257. https://doi.org/10.1190/geo2015-0281.1.

Revil, A., Soueid, Ahmed A., Jardani, A., 2017. Self-potential: a non-intrusive ground water flow sensor. J. Environ. Eng. Geophys. 22 (3), 235–247. https://doi.org/10.2113/JEEG22.3.235.

Richards, K., Revil, A., Jardani, A., Henderson, F., Batzle, M., Haas, A., 2010. Pattern of shallow ground water flow at Mount Princeton Hot Springs, Colorado, using geoelectrical methods. J. Volcanol. Geotherm. Res. 198, 217–232. https://doi.org/10.1016/j.jvolgeores.2010.09.001.

Rittgers, J.B., Revil, A., Karaoulis, M., Mooney, M.A., Slater, L.D., Atekwana, E.A., 2013. Self-potential signals generated by the corrosion of buried metallic objects with application to contaminant plumes. Geophysics 78 (5). https://doi.org/10.1190/GEO2013-0033.1. EN65-EN82.

Sato, M., Mooney, H.M., 1960. The electrochemical mechanism of sulfide self-potentials. Geophysics 25, 226–249. https://doi.org/10.1190/1.1438689.

Semenov, A.S., 1980. Elektrorazvedka Metodom Estestvennogo Elektricheskogo Polia, 2nd ed. 445 pp., Nedra, Leningrad, Russia.

Sheffer, M., 2007. Forward Modeling and Inversion of Streaming Potential for the Interpretation of Hydraulic Conditions from Self-Potential Data. PhD thesis,. The University of British Columbia.

Sheffer, M.R., Howie, J.A., 2003. A numerical modelling procedure for the study of the streaming potential phenomenon in embankment dams. In: Symposium on the Application of Geophysics to Engineering and Environmental Problems, San Antonio, pp. 475–487.

Sill, W.R., 1983. Self-potential modeling from primary flows. Geophysics 48, 76–86.

Sinmyo, R., Keppler, H., 2016. Electrical conductivity of NaCl-bearing aqueous fluids to 600 °C and 1 GPa. Contrib. Mineral. Petrol. 172 (1), 4. https://doi.org/10.1007/s00410-016-1323-z.

Soueid Ahmed, A., Jardani, A., Revil, A., Dupont, J.P., 2016. Specific storage and hydraulic conductivity tomography through the joint inversion of hydraulic heads and self-potential data. Adv. Water Resour. 89, 80–90. https://doi.org/10.1016/j.advwatres.2016.01.006.

Soueid, Ahmed A., Jardani, A., Revil, A., Dupont, J.P., 2016. Joint inversion of hydraulic head and self-potential data associated with harmonic pumping tests. Water Resour. Res. 52, 6769–6791. https://doi.org/10.1002/2016WR019058.

Spies, B.R., Frischknecht, F.C., 1992. Electromagnetic sounding. In: Nabighiam, M.N. (Ed.), Electromagnetic Methods in Applied Geophysics, vol. 2. SEG, pp. 285–426.

Stoll, J., Bigalke, J., Grabner, E., 1995. Electrochemical modelling of self-potential anomalies. Surv. Geophys. 16, 107–120. https://doi.org/10.1007/BF00682715.

Su, Z., Tao, C., Zhu, Z., Revil, A., Shen, J., Nie, Z., Li, Q., Deng, X., Zhou, J., Liu, L., 2022. Joint interpretation of marine self-potential and transient electromagnetic survey for seafloor massive sulfide (SMS) deposits: Application at TAG hydrothermal mound, Mid-Atlantic Ridge. J. Geophys. Res. Solid Earth 127. https://doi.org/10.1029/2022JB024496 e2022JB024496.

Suski, B., Rizzo, E., Revil, A., 2004. A sandbox experiment of selfpotential signals associated with a pumping test. Vadose Zone J. 3, 1193–1199. https://doi.org/10.2136/vzj2004.1193.

Suski, B., Revil, A., Titov, K., Konosavsky, P., Dagès, C., Voltz, M., Huttel, O., 2006. Monitoring of an infiltration experiment using the self-potential method. Water Resour. Res. 42, W08418. https://doi.org/10.1029/2005WR004840.

Titov, K., Revil, A., Konosavsky, P., Straface, S., Troisi, S., 2005. Numerical modelling of self-potential signals associated with a pumping test experiment. Geophys. J. Int. 162 (2), 641–650. https://doi.org/10.1111/j.1365-246X.2005.02676.x.

Villasante-Marcos, V., Finizola, A., Abella, R., Barde-Cabusson, S., Blanco, M.J., Brenes, B., Cabrera, V., Casas, B., De Agustín, P., Di Gangi, F., Domínguez, I., García, O., Gomis, A., Guzmán, J., Iribarren, I., Levieux, G., López, C., Luengo, N., Martín, I., Moreno, M., Meletlidis, S., Morin, J., Moure, D., Pereda, J., Ricci, T., Romero, E., Schütze, C., Suski-Ricci, B., Torres, P., Trigo, P., 2014. Hydrothermal system of Central Tenerife Volcanic Complex, Canary Islands (Spain), inferred from self-potential measurements. J. Volcanol. Geotherm. Res. 272, 59–77. https://doi.org/10.1016/j.jvolgeores.2013.12.007.

Vozoff, K., 1992. The magnetotelluric method. In: Nabighiam, M.N. (Ed.), Electromagnetic Methods in Applied Geophysics, vol.2. SEG, pp. 641–712. https://doi.org/10.1190/1.9781560802686.ch8.

Watanabe, N., Yamaya, Y., Kitamura, K., Mogi, T., 2021. Viscosity-dependent empirical formula for electrical conductivity of H_2O-NaCl fluids at elevated temperatures and high salinity. Fluid Phase Equilib. 549, 113187 https://doi.org/10.1016/j.fluid.2021.113187.

Waxman, M.H., Smits, L.J.M., 1968. Electrical conductivities in oil-bearing shaly sands. Soc. Pet. Eng. J. 8 (2), 107–122. https://doi.org/10.2118/1863-A.

Wilt, M.J., Corwin, R.F., 1989. Numerical modeling of self-potential anomalies due to leaky dams: Model and field examples. In: Lecture Notes in Earth Sciences, 27, ed. G. P. Merkler et al., Detection of subsurface flow phenomena. Springer-Verlag, Berlin Heidelberg, pp. 73–89. https://doi.org/10.1007/BFb0011631.

Wurmstich, B., Morgan, F.D., 1994. Modeling of streaming potential responses caused by oil well pumping. Geophysics 59, 46–56. https://doi.org/10.1190/1.1443533.

Yamashita, S., 1961. The electromotive force generated within the ore body by the temperature difference. J. Min. Coll. Akita Univ. Ser. A 1, 69.

Yasukawa, K., Bodvarsson, G., Wilt, M., 1993. Coupled self-potential and mass-heat flow code for geothermal applications. Trans. Geotherm. Resour. Council 17, 203–207.

Yasukawa, K., Mogi, T., Widarto, D., Ehara, S., 2003. Numerical modeling of a hydrothermal system around Waita volcano, Kyushu, Japan, based on resistivity and self-potential survey results. Geothermics 32 (1), 21–46. https://doi.org/10.1016/S0375-6505(02)00048-2.

Yasukawa, K., Ishido, T., Suzuki, I., 2005. Geothermal reservoir monitoring by continuous self-potential measurements, Mori geothermal field, Japan. Geothermics 34 (5), 551–567. https://doi.org/10.1016/j.geothermics.2005.04.005.

Zhu, Z., Tao, C., Shen, J., Revil, A., Deng, X., Liao, S., Zhou, J., Wang, W., Nie, Z., Yu, J., 2020. Self-potential tomography of a deep-sea polymetallic sulfide deposit on Southwest Indian Ridge. J. Geophys. Res. Solid Earth 125. https://doi.org/10.1029/2020JB019738 e2020JB019738.

Zlotnicki, J., Nishida, S., 2003. Review on morphological insights of self-potential anomalies on volcanoes. Surv. Geophys. 24 (4), 291–338. https://doi.org/10.1023/B:GEOP.0000004188679 23.ac.

Zohdy, A.A.R., Anderson, L.A., Mufler, L.J.P., 1973. Resistivity, self-potential and induced-polarization surveys of a vapourdominated geothermal system. Geophysics 38, 1130–1144. https://doi.org/10.1190/1.1440400.